QUALIFICATION EXAM REPORT: DISPERSION-CORRECTED DFT APPLIED TO SURFACE CHEMISTRY AND LAYERED-MATERIAL HETEROSTRUCTURES

by

Alastair J. A. Price

Submitted in partial fulfillment of the requirements
for the degree of Doctor of Philosophy

at

Dalhousie University
Halifax, Nova Scotia
August 2020

© Copyright by Alastair J. A. Price, 2020

CONTENTS

List of Tables . . . . . **iv**

List of Figures . . . . . **v**

List of Abbreviations and Symbols Used . . . . . **vi**

Abstract . . . . . **xi**

Chapter 1 Introduction: Dispersion in Solids **1**

Chapter 2 Theory **6**

2.1 Density-Functional Theory 6

2.2 Periodic Boundary Conditions in the Solid State 9

2.3 Planewaves and Pseudopotentials 11

2.4 All-Electron Methods and Basis Sets 15

2.5 The Exchange-Hole Dipole Moment Dispersion Model 19

2.6 Alternative Post-SCF Dispersion Methods 23

2.6.1 The Grimme-D Series of Dispersion Models 23

2.6.2 The TS and MBD Methods 25

2.6.3 Non-Local van der Waals Functionals 26

Chapter 3 Interpreting Surface-Adsorption Chemistry from STM Images Generated Via Dispersion-Corrected DFT **28**

3.1 Previous Work 28

3.2 Scanning Tunnelling Microscopy Theory 30

3.3 Computational Methods 31

3.4 Results and Discussion 32

3.4.1 STM Images 32
3.4.2 Binding Energies 36

3.5 Conclusions 37

Chapter 4 Proposal **39**

4.1 Transition Metal Dichalcogenides and their Interfaces 39

4.2 FHIaims Timings and Applications 43

4.3 Dispersion in Layered Solids 47

4.4 Proposed Work 49
4.4.1 XDM Implementation in FHIaims 49
4.4.2 Application to TMDC Interfaces 52

Bibliography **55**

LIST OF TABLES

2.1 Valence configuration and core-region cutoff radii, r_c, in atomic units for the B86bPBE PAW datasets used in this work. 14

2.2 Minimum bond distances from optimized geometries in this work, compared to the sum of maximum core cutoff radii for each element. 15

3.1 Binding energies for the Fe-tpy species, along with the base-functional and XDM dispersion contributions. 36

4.1 Averaged C_6 dispersion coefficients used for the Tawfik subset of 11 layered materials. 49

LIST OF FIGURES

1.1 Potential energy curve for graphite exfoliation. 2

2.1 A schematic representation of the PAW method. 13

3.1 Minimum-energy geometry of the Fe-terpyridine complex on the Ag(111) surface, along with simulated and reference experimental STM images. 32

3.2 Low-energy structures of CO and C_2H_4 coordinated with the adsorped Fe-tpy complex, along with simulated and reference experimental STM images. 34

4.1 The molybdenum disulfide (MoS_2) unit cell 40

4.2 Potential plots for graphene on a 6-layer Ni surface computed with B86bPBE-XDM. 42

4.3 Sketch of the three most common interface types for top contact metal-TMDC interfaces 43

4.4 Time in hours taken for a single SCF energy evaluation for Quantum ESPRESSO and FHIaims for MoS_2 cells of increasing size. 45

4.5 Time in hours taken for a single SCF energy evaluation for Quantum ESPRESSO and FHIaims for a 5×5 bulk of MoS_2 for various numbers of CPUs. 46

4.6 Summary of dispersion-corrected DFT errors for layered materials 48

List of Abbreviations and Symbols Used

Abbreviation	Description
a.u.	Atomic Unit
AE	All-Electron
APW	Augmented Planewave Method
ATM	Axilrod-Teller-Muto Three-Body Dispersion-Energy Term
B86bPBE	Becke's B86b Exchange and PBE GGA Density Functional
BE	Binding Energy
BJ	Becke-Johnson
BR	Becke-Roussel
BSSE	Basis-Set Superposition Error
CP	Counterpoise
CPU	Computer Processing Unit
DFT(-D)	(Dispersion-Corrected) Density-Functional Theory
Dn	Grimme's Series of Dispersion Corrections (e.g., n= 2, 3, 4)
DNA	Deoxyribonucleic Acid
Expt	Experimental
gCP	Geometrical Counterpoise Method
GGA	Generalized-Gradient Approximation
GTO	Gaussian-Type Orbitals
FHIaims	Fritz Haber Institute *ab initio* molecular simulations
HF	Hartree-Fock Theory
HSE06	Heyd-Scuseria–Ernzerhof Variable Exchange Hybrid Functional
KB(49)	Kannemann-Becke Benchmark Set of Molecular Dimers
KS	Kohn and Sham
LAPW	Linearised Augmented Planewave Methods
LSDA	Local Spin Density Approximation
MBD	Many-Body Dispersion Model
MP	Monkhorst-Pack k-point Grid Sampling Scheme
NAO	Numerical Atomic Orbitals
PAW	Projector-Augmented Wave

Abbreviation	Description
PBE	Perdew-Burke-Ernzerhof Density GGA Density Functional
PBE0	Perdew-Burke-Ernzerhof Hybrid Density Functional
PP	Pseudopotential
QE	Quantum ESPRESSO
rVV10	Revised Vydrov and van Voorhis Non-Local Density Functional
S12L	Grimme's Set of Large Complexes
S22	Set of Non-Covalent Complexes
SCF	Self-Consistent Field
SCS	Self-Consistent Screening
STM	Scanning Tunnelling Microscopy
STS	Scanning Tunnelling Spectroscopy
STO	Slater-Type Orbitals
TMDC	Transition Metal Dichalcogenides
TS	Tkatchenko-Scheffler Dispersion Model
vdW	van der Waals
VV	Vydrov and van Voorhis
X23	Benchmark Set of Molecular Organic Solids
XDM	Exchange-Hole Dipole Moment Dispersion Model

Symbol	Description
a, b, c	Unit Cell Parameters
a_1, a_2	XDM Becke-Johnson Damping Parameters
a_x	Fraction of Exact Exchange
$\mathbf{a}$	Unit Cell Vector
A, a, b	Becke-Roussel Exchange-Hole Parameters
$\mathbf{b}$	Reciprocal Cell Vector
$c_{\mathbf{k+R}}$	Fourier Coefficient
$C_{n,a}$	Homoatomic Dispersion Coefficient (e.g., n = 6, 8, 10)
$C_{n,ab}$	Two-Body Dispersion Coefficient (e.g., n = 6, 8, 10)
CN	Coordination Number in D3 Dispersion Model
c_x	Constant Defined in LSDA and GGA Exchange Energy Expressions
d, d_1, d_2	Damping Parameters Used in D2 and D3 Dispersion Models
$d_{X\sigma}$	Exchange-Hole Dipole Moment
E_c	Correlation Energy

Symbol	Description
E^{cut}	Planewave Kinetic-Energy Cutoff
E_{disp}	Dispersion Energy
E_{DFT}	Total DFT Energy
E_{ex}	Exfoliation Energy
$E_{\mathrm{x}}^{\mathrm{GGA}}$	GGA Exchange Energy
$E_{\mathrm{x}}^{\mathrm{LSDA}}$	LSDA Exchange Energy
E_{latt}	Lattice Energy
E^{nl}	Non-Local Energy
E_{x}	Exchange Energy
$E_{\mathrm{x}}^{\mathrm{HF}}$	Hartree-Fock Exact Exchange Energy
$E_{\mathrm{x}}^{\mathrm{hybrid}}$	Hybrid Exchange Energy
E_{xc}	Exchange-Correlation Energy
E_{μ}	Energy of State Without Tunnelling
$f(E)$	Fermi Function
$f(R_{ab\mathbf{L}})$	Damping Function
$\mathbf{G}$	Reciprocal Lattice Vector
$\hat{H}$	Electronic Hamiltonian
$\hbar$	Reduced Planck's Constant
$h_{X\sigma}$	Spin-Dependant Exchange Hole
i, j	Electronic Index
$\mathrm{I}_{\mathrm{A,B}}$	Atomic Ionization Energies
J	Classical Coulomb self energy
$\mathbf{k}$	Reciprocal Space Vector
∇^2	Laplacian Operator
m	Atomic Mass
M_l	l-th Order Multipole Moment
$M_{\mu\nu}$	Tunnelling Matrix Elements
N	Normalization Factor or Number
$\tilde{p}_i$	Projector Functions
e	Electron Charge
$\mathbf{q}$	Reciprocal Space Vector
Q_{σ}	Exchange Hole Curvature
r	Radius
r_{12}	Interelectronic Separation

Symbol	Description
r_c	Radial Cutoff
r_{cl}	Radial Cutoff with Angular Momentum l
$\mathbf{R}$	Bravais Lattice Vector
R_{ab}	Interatomic Distance
$R_{ab\mathbf{L}}$	Interatomic Distance in a Periodic System
R_{vdW}	van der Waals Radius
s	Dimensionless Reduced Density Gradient
s_{42}	Scaling Factor Used in D3 Dispersion Model
s_6	Damping Parameter Used in D2 and D3 Dispersion Models
s_8	Damping Parameter Used in D3 Dispersion Model
s_r	Damping Parameter Used in TS Dispersion Model
$S_{n,n'}$	Overlap Matrix of Basis Functions
$\hat{T}$	Transform Operator for PAW method
T_{KS}	Kinetic-Energy of Non-Interacting Electrons
$u(r)$	Radial Function of NAOs
$\hat{U}$	Electron-Electron Interaction Energy
$\mathcal{V}$	Periodic Potential
V	Volume
V_{ext}	External Potential
Y_{lm}	Spherical Harmonics for Basis Sets
α_a	Atom-in-Solid Polarizability
α_a^{at}	Free-Atom Polarizability
β	Constant Defined in B86bPBE Enhancement Factor Expression
γ	Constant Defined in B86bPBE Enhancement Factor Expression
Γ	Brillouin-Zone Center
δ_{ij}	Kronecker Delta
ϵ	Potential Well Depth
ε_i	Orbital Energy
ε_{x}	Exchange Energy Density
ζ	Gaussian Exponential Coefficient
η,ξ	Cartesian Directions
κ	Constant Defined in PBE Enhancement Factor Expression
ρ	Electron Density

Symbol	Description
μ	Constant Defined in PBE Energy and Enhancement Factor Expressions
$\mu\,\nu$	Atom-Orbital Indices
$\mu_{A,B}$	Dipole Moment Integral
σ	Electron Spin Index
σ_{disp}	van der Waals Contribution to Cell Stress
τ_σ	Positive-Definite Spin-Kinetic-Energy Density
ϕ	Atomic Orbital
$\tilde{\phi}$	Pseudo Partial Wave
Φ	Non-Local Correlation Kernel
φ	Basis Functions
ψ	Electronic Wavefunction
Ψ	Total Electronic Wavefunction
$\tilde{\Psi}$	Pseudised Wavefunction
ψ_{k}	Bloch Wavefunction
ω_{Hirsh}	Hirshfeld Weight

ABSTRACT

Dispersion forces are a type of long-range interaction ubiquitous in chemistry. Including dispersion forces is key to the correct computational prediction of the structure of biomolecules, molecular self-assembly, surface adsorption, and properties of layered materials. Dispersion-corrected density-functional theory (DFT-D) is a tool that has become efficient and accurate enough for the study of surface adsorption and of interfaces containing layered materials, amongst other applications. In this work, we apply the exchange-hole dipole moment (XDM) dispersion correction to study adsorption of iron-terpyridine, and its complexes with carbon monoxide and ethylene, on Ag(111) metal surfaces. Layered materials will be the focus of the proposed work and are an interesting class of materials, which have the potential to revolutionize computing and optoelectronic devices. These materials, although exciting, still have some notable barriers preventing potential future application. The proposed work focuses on the application of the XDM method to study a subclass of layered materials, called transition metal dichalcogenides (TMDC), and their heterojunctions. TMDCs are of particular interest due to their stability and their tunable band gaps, controlled via varying the number of atomically-thin layers. Theoretical study of TMDC heterojunctions has previously been difficult due to scaling penalties that arise in many solid-state codes employing planewave basis sets, as well as accuracy issues due to the use of empirical dispersion methods, which do not correctly capture the dispersion interactions that occur within TMDC heterojunctions. We propose that the implementation of XDM within the linear scaling-Fritz Haber Institute *ab initio* molecular simulations (FHIaims) electronic-structure code package will allow for the accurate and computationally efficient study of TMDC heterojunctions.

CHAPTER 1

INTRODUCTION: DISPERSION IN SOLIDS

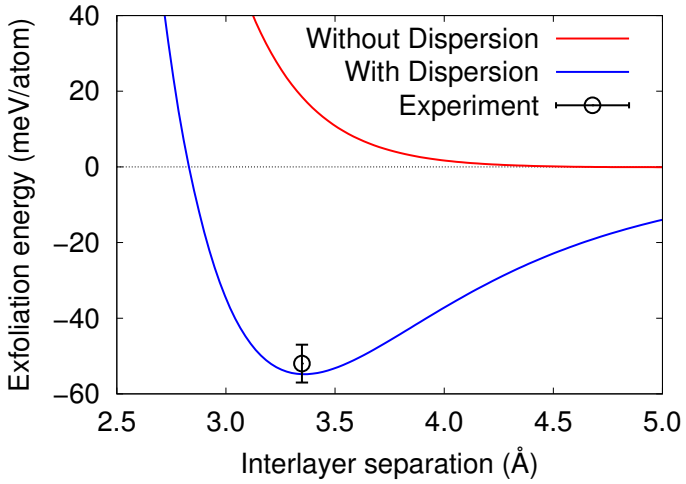
Modern density-functional theory (DFT)[1,2] has its origins in 1964–1965 works by Hohenberg, Kohn, and Sham.[3,4] They showed that the total electron density, ρ, completely describes all ground state properties of an N-electron system, which simplifies the complexity down to a function of three coordinates independent of the number of electrons.[1] The variational principle must also be applied, where the density that minimizes the total energy is the exact ground state density.[1,3] The breakthroughs in the works by Hohenberg, Kohn, and Sham ultimately allow one to write the total energy functional of the electron density as

$$E(\rho) = T_{\mathrm{KS}}(\rho) + \int V_{\mathrm{ext}} d\boldsymbol{r} + J(\rho) + E_{\mathrm{xc}}(\rho), \tag{1.1}$$

where $T_{\mathrm{KS}}(\rho)$ is the kinetic energy of the non-interacting electrons, V_{ext} is the external potential from the nuclear charges, $J(\rho)$ is the classical Coulomb self-energy, and the only unknown term is the exchange-correlation functional, E_{xc}.[1] Much of the DFT work since 1965 has focused on the development of newer and more accurate functionals for E_{xc}.[1,2]

Modern DFT allows for the modelling of electronic structure of both molecules and solid materials. DFT is widely used across computational chemistry, physics, and materials science in order to investigate the fundamental nature of interactions in matter, which aid in the interpretation and prediction of experimental results. The power of DFT has helped in the design of new drugs, reactions, catalysts, and materials, amongst many other things.[1,2,5–7] While DFT has been shown to be highly accurate for most examples of intramolecular chemistry, its applications to problems in intermolecular chemistry are still not as developed. A key issue with DFT is that many of the original exchange-correlation functionals are based on the local- (local density approximation) or the semi-local-density (generalized-gradient approximation) and, by definition, neglect all non-local

Figure 1.1: Potential energy curve for graphite exfoliation using B86bPBE-XDM[17–19] for graphite with dispersion and B86bPBE[17,18] without dispersion, computed as described in Ref. 19



interactions. This leads to inaccuracies by many density-functionals for the modelling of systems involving London dispersion, which is a wholly non-local type of electron correlation.

London dispersion[8,9] interactions are long-range interactions that arise between instantaneous dipole (and higher-order multipole) moments in the electron distribution of atoms or molecules. These instantaneous dipoles arise from time-dependent variation of the electron distribution around the nuclei, and these changes in density can create instantaneous electric fields. These electric fields are in turn felt by neighbouring atoms or molecules around this instantaneous dipole and induce further density polarization, resulting in an attractive force. London dispersion is the driving force behind the condensation of non-polar molecules and, despite being the weakest intermolecular interaction, is ubiquitous in chemistry. London dispersion forces are key to determining the 3D structure of biomolecules such as proteins and DNA,[10] molecular self-assembly,[11] interactions within layered materials such as the carbon sheets of graphene to make graphite,[12] surface adsorption,[13] phase transitions,[14] and molecular crystal packing.[8,15,16]

The importance of dispersion for layered materials can be seen in the potential energy curves for the exfoliation of graphite, as seen in Fig. 1.1. Without the inclusion of dispersion, graphene layers are not predicted to bind together. However, with the inclusion of a dispersion correction, DFT instead predicts an interlayer separation and exfoliation energy that match experiment.[20] There are currently a number of distinct methods to address the lack of dispersion forces within the base DFT functional.[19,21]

Consider two non-polar atoms A and B. The dispersion energy between these two atoms can be determined from second-order perturbation theory, where the non-interacting atomic wave

functions are used as the unperturbed reference state and the dispersion forces are treated as a small perturbation.[19,22–24] As the atoms are non-polar, they have no permanent dipoles and the first order energy correction can be shown to be zero.[22–24] Therefore one must look at the second-order correction to describe dispersion forces. Using the closure approximation,[24,25] which avoids the explicit sum over excited atomic states, the second-order dispersion energy (in atomic units) is

$$E^{(2)} \approx -\frac{2}{3}\left(\frac{1}{\Delta E_A + \Delta E_B}\right)\frac{\left\langle \mu_A^2 \right\rangle \left\langle \mu_B^2 \right\rangle}{R_{ab}^6}, \tag{1.2}$$

where R is the internuclear separation, $\left\langle \mu^2 \right\rangle$ is the dipole moment integral, and ΔE is the average excitation energy. In the absence of a permanent dipole moment, $\left\langle \mu_A^2 \right\rangle \approx \frac{3}{2}\alpha_A \Delta E_A$ due to the relationship between the mean-square dipole moment and the polarizability. Also, $\Delta E_{A,B}$ can be replaced by taking the average excitation energies as roughly equal to the atomic ionization potentials, $I_{A,B}$. This substitution gives rise to the London formula,[24]

$$E^{(2)} \approx -\frac{3}{2}\left(\frac{I_A I_B}{I_A + I_B}\right)\frac{\alpha_A \alpha_B}{R^6}, \tag{1.3}$$

which simplifies the dispersion energy down to an expansion in terms of the atomic ionization energies, $I_{A,B}$, and polarizabilities, $\alpha_{A,B}$. Although approximate, it begins to allow an understanding of the true physics of dispersion interactions. The London formula, for example, correctly predicts that atoms with large polarizabilites have the greatest interatomic dispersion interactions.

An early way of modelling dispersion interactions was through the use of a Lennard-Jones potential.[26] The Lennard-Jones potential consists of two fundamental parts: a steep repulsive R^{-12} term and a smooth attractive R^{-6} term. It is represented by the following potential:

$$V(R) = 4\epsilon\left[\left(\frac{\sigma}{R}\right)^{12} - \left(\frac{\sigma}{R}\right)^{6}\right], \tag{1.4}$$

where ϵ represents the potential well depth or strength of the interaction between two particles, and σ represents the sum of van der Waals radii of the particles. Although simplistic in its formulation, the Lennard-Jones potential is still in use today in force field calculations, with empirical atom typing for the dispersion coefficients.[27–29]

Building on the insight gained from second-order perturbation theory, a number of methods have been formulated to address the missing component of dispersion within DFT. These can be broken down into two key categories: dispersion corrections and dispersion-including functionals. These

two types further can be subdivided into asymptotic dispersion corrections,[19,30–42] dispersion-correcting potentials,[43–49] non-local functionals,[41,42,50–54] parameterized exhange-correlation functionals,[55–59] and others.[36,60,61]

The focus of this work is on the subclass of asymptotic dispersion corrections. This subclass is attractive as asymptotic dispersion corrections are simple in their formulation and capable of high accuracy, whilst also being low in computational cost when compared to other types of dispersion methods. In a general asymptotic dispersion correction, the leading-order dispersion energy term is represented as

$$E_{\text{disp}}^{(6)} = -\sum_{i<j} \frac{C_{6,ij} f_{6,ij}(R_{ij})}{R_{ij}^6}, \tag{1.5}$$

where the sum runs over all atomic pairs and the $C_{6,ij}$ are the interatomic dispersion coefficients which can be approximated, for example, by the London formula above. In order to ensure physicality, the dispersion energy is damped by some function, $f_{6,ij}(R_{ij})$, at short internuclear distances to avoid divergence.

Commonly employed asymptotic dispersion corrections include Grimme's D2,[30] D3,[31,32] and D4 models,[33,34] the Tkatchenko-Scheffler (TS)[35] method, and the exchange-hole dipole moment correction (XDM)[19,62] of Becke and Johnson. The difference in each correction arises from the method by which the C_6 term is calculated and whether higher-order dispersion terms, such as C_8 or C_{10}, are included. For example, the early D2 implementation of Grimme's series of corrections was limited to the C_6 term and used fixed parameterized values for the dispersion coefficients. The later D3 correction computes the C_6 terms using coordination numbers and also includes C_8. XDM improves on the accuracy of the dispersion energy through the inclusion of both C_8 and C_{10} terms, and the dispersion coefficients are calculated from the electron density, which allows the correction to respond robustly to a wide range of chemical environments.

Currently, XDM is only implemented in a limited selection of codes, and is not available within the Fritz Haber Institute *ab initio* molecular simulations package (FHIaims).[63–69] The relatively recent development of the FHIaims code is a key advancement that will be leveraged for the work proposed in this report. FHIaims is an all-electron electronic-structure code package, with both molecular and solid-state application. It uses numerical atomic orbitals (NAOs) as basis set functions, which allows computational flexibility and speed not seen with planewave codes for periodic solids. The flexibility and speed from NAOs arises due to the fact that they are localized around atoms, allowing them to be truncated in space beyond a given distance, and the number of basis functions needed to converge the system is usually smaller than with other competing methods.[70] The computational efficiency of FHIaims paired with XDM will allow for the study of very large (> 200 atoms) solid-state systems, such as 2D layered material-based heterojunctions,

that would previously have been impractical with conventional planewave codes. Furthermore, FHIaims is able to extend the range of applicability of hybrid-functionals to solids, which have been too computationally expensive or impractical for planewave-based codes (except for small unit cells, of ~ 10 atoms or less), and with greater accuracy than can be attained with minimal Gaussian basis sets in the CRYSTAL code.[71,72]

The purpose of the proposed work is the implementation and testing of the XDM model within the FHIaims code. The new FHIaims-XDM code will be rigorously benchmarked against conventional systems from the literature (the Kanneman-Becke 49 set of intermolecular complexes[73] and the X23 set of molecular crystals[19,74,75]), with the intent to compare the XDM module's performance head-to-head with other commonly employed dispersion corrections. Once the performance of the XDM module has been demonstrated, it will be tested on a benchmark set of layered materials,[76,77] as such materials are the main focus of this proposed work. Layered materials, such as transition metal dichalcogenides (TMDCs), are of interest as they are a potential new avenue for device technologies in a post-silicon world.[78–83] These materials, although promising, still have fundamental issues to overcome, such as charge mobility at metal-TMDC heterojunctions.[78–82] The XDM module paired with FHIaims will allow accurate and computationally tractable modelling of device structure and bonding. XDM's accurate treatment of dispersion will allow for the further investigation of charge transfer and the effect which the tunnelling barrier plays at metal-TMDC heterojunctions.

This report will focus on the application of XDM-corrected DFT to solid-state systems involving layered materials and metal surfaces. Chapter 2 will start with a detailed description of DFT and the forms of the exchange-correlation functionals to be used in this work. The considerations of how periodic boundary conditions affect solid-state DFT calculations will also be discussed. Following this, an overview of planewaves and pseudopotentials will be given, as they have been both used for the existing solid-state implementation. Next, all-electron methods and basis sets will be discussed. The last section within Chapter 2 will be a review of dispersion methods, with a detailed description of the XDM method, as well as outlines of Grimme's methods and the Tkatchenko-Scheffler and Many-Body Dispersion corrections. Chapter 3 will then describe a completed computational research project that investigates surface adsorption through XDM-corrected DFT to enable theoretical assignment of structures characterized experimentally by scanning tunnelling microscopy (STM) and will directly apply the theory discussed in Chapter 2. Finally, Chapter 4 will outline the proposed research project, which contains the implementation and use of XDM in the FHIaims electronic-structure code, as well as its proposed use to study heterojunctions containing TMDCs.

CHAPTER 2

THEORY

2.1 Density-Functional Theory

Density-functional theory (DFT)[1,2] is fundamentally a quantum-mechanical modelling method underpinned by the time-independent Schrödinger equation,[84]

$$\hat{H}\psi = E\psi. \tag{2.1}$$

Here, E is the energy, $\psi(\mathbf{r}_1, \ldots, \mathbf{r}_N)$ is the N-electron wavefunction, and $\hat{H}$ is the Hamiltonian,

$$\hat{H} = \hat{T} + \hat{V} + \hat{U}, \tag{2.2}$$

shown here broken into its kinetic energy term ($\hat{T}$), the external potential energy term ($\hat{V}$), and the electron-electron interaction energy ($\hat{U}$).

DFT is used in many branches of chemistry and physics to answer fundamental questions concerning the electronic structure of many-body systems, in the forms of atoms, molecules, or condensed phases.[1,2,5,85,86] DFT does not directly solve the time-independent Schrödinger equation, but instead systematically maps the many-body problem onto a single-particle problem with the key variable being the electronic density, $\rho(\mathbf{r})$, given by

$$\rho(\mathbf{r}) = \int \cdots \int \psi^*(\mathbf{r}_1, \ldots, \mathbf{r}_N)\psi(\mathbf{r}_1, \ldots, \mathbf{r}_N) d\mathbf{r}_1, \ldots d\mathbf{r}_N. \tag{2.3}$$

DFT was made practical by the work by Kohn and Sham in 1965.[87] The fundamental assumption of Kohn and Sham is that the exact ground-state density can be obtained from numerical solution of a set of single-particle Schodinger-like equations for a system of non-interacting electrons.[87]

The total energy functional for a Kohn-Sham system can be written as

$$E[\rho] = \int v_{\text{ext}}(\mathbf{r})\rho(\mathbf{r})d\mathbf{r} + J[\rho] + T_s[\rho] + E_{\text{xc}}[\rho], \tag{2.4}$$

where v_{ext} is the external potential that arises from the electron-nuclei interactions,

$$J[\rho] = \frac{1}{2}\int\int \frac{\rho(\mathbf{r})\rho(\mathbf{r}')}{|\mathbf{r}-\mathbf{r}'|}d\mathbf{r}d\mathbf{r}' \tag{2.5}$$

is the Hartree or classical Coulomb energy between electrons, and T_s is the kinetic energy, which can be written in terms of the Kohn-Sham orbitals as

$$T_s[\rho] = \sum_{i=1}^{N}\int \phi_i^*(\mathbf{r})\left(-\frac{1}{2}\nabla^2\right)\phi_i(\mathbf{r})d\mathbf{r}, \tag{2.6}$$

where ∇^2 is the Laplacian operator. Lastly, E_{XC} is the exchange-correlation energy, which contains all of the energetic contributions neglected by the other terms.

In practice Equation 2.4 must be solved in an iterative or self-consistent fashion. This is done through the self-consistent field (SCF) procedure, as in Hartree-Fock theory, which obtains the orbitals that minimize the energy of the system. This occurs through variationally lowering the electronic energy by optimizing the electron density. The density is constructed from the occupied Kohn-Sham orbitals as

$$\rho(\mathbf{r}) = \sum_{i}^{N}|\phi_i(\mathbf{r})|^2. \tag{2.7}$$

The Kohn-Sham equations are then solved for the energy and an updated set of Kohn-Sham orbitals. This iterative process is continued until the energy is converged to within a certain tolerance and the procedure is finished.

As mentioned earlier, it is the E_{xc} term in Equation 2.4 where all previously neglected energetic components are packaged. Since the exact form of E_{xc} is not known, there have been many different density-functional approximations proposed over the years of DFT.[1,2] The exchange-correlation energy can be separated into its component parts, exchange energy (E_{x}) and correlation energy (E_{c}), as $E_{\text{xc}} = E_{\text{x}} + E_{\text{c}}$. From this point onwards, only the form of exchange functional will be directly discussed, as its contribution to E_{xc} energy is far greater than that of E_{c}.[1]

The first and simplest exchange functional is the local spin density approximation (LSDA), which the has the form

$$E_{\text{x}}^{\text{LDSA}} = -\frac{3}{2}\left(\frac{3}{3\pi}\right)^{1/3}\sum_{\sigma}\int \rho_\sigma^{4/3}(\mathbf{r})d\mathbf{r}, \tag{2.8}$$

where the sum is over electron spins and ρ_σ is the spin-dependent density. The correlation energy for the LSDA is obtained from quantum Monte Carlo calculations on the uniform electron gas, as there is no closed-form expression.[88] The LSDA typically leads to an underestimation of the exchange energies and an over-estimation of correlation and bond energies.[1] This lead to the first improvement on the LSDA and spawned a class of functionals called generalized gradient approximations (GGA).

Real chemical systems do not contain a uniform-electron-gas type density. For GGA-type functionals, the exchange energy depends on both the density and the density gradient, $\nabla\rho$, and has the general form

$$E_{\mathrm{x}}^{\mathrm{GGA}} = \sum_{\sigma} \int \varepsilon_{\mathrm{x}}(\rho_\sigma, \nabla\rho_\sigma) d\mathbf{r}. \tag{2.9}$$

where ε_{x} is the exchange-energy density. Two common GGAs used in this work are the Becke86b (B86b)[17] and Perdew-Burke-Ernzerhof (PBE)[18] exchange functionals. These GGAs have the form

$$E_{\mathrm{X}}^{\mathrm{GGA}} = -\sum_{\sigma} \int c_{\mathrm{x}} \rho_\sigma^{4/3} F(\chi_\sigma) d\mathbf{r}, \tag{2.10}$$

where $F(\chi_\sigma)$ is termed the enhancement factor, c_{x} a constant term and χ_σ is the dimensionless density gradient,

$$\chi_\sigma = \frac{\nabla\rho_\sigma}{\rho_\sigma^{4/3}}. \tag{2.11}$$

The differences between PBE and B86b arise in the enhancement factor, where PBE has the form[89]

$$F(\chi_\sigma) = 1 + \frac{\beta}{c_{\mathrm{x}}} \frac{\chi_\sigma^2}{1 + \gamma\chi_\sigma^2}, \tag{2.12}$$

whose two parameters β and γ arise from imposing known constraints.[18] This functional corrects for the uniform-electron gas in the low-gradient limit, but misses the correct behaviour in the large-gradient limit.[17] The B86b functional was developed to address the large gradient limit. It has the same form for the exchange energy as in Equation 2.10, but the enhancement factor is different:

$$F(\chi_\sigma) = 1 + \frac{\beta}{c_{\mathrm{x}}} \frac{\chi_\sigma^2}{(1 + \gamma\chi_\sigma^2)^{4/5}}. \tag{2.13}$$

In the case of B86b, the parameters β and γ were fit to atomic exchange energies.[17] Both PBE and B86b exchange are typically paired with the PBE correlation functional.[18] PBE is generally the most widely used density functional for solid-state applications.[2,18] However, B86bPBE[17,18] is our functional of choice in this work due to its behaviour in the large-gradient limit, which ensures better performance for non-bonded repulsion.[90,91]

GGAs represent major improvements over the LSDA for many systems of chemical interest, but are still limited in their performance as they are semi-local. More complicated classes of functionals include meta-GGAs[92] and hybrid functionals,[93] which can achieve greater chemical accuracy.[1] For meta-GGAs, this is achieved through the additional inclusion of the kinetic energy density, τ_σ, and the Laplacian of the density, $\nabla^2\rho_\sigma$,[92] with more information given in Section 2.5. Moving beyond GGAs and meta-GGAs, exact (HF) exchange may be included to give a hybrid functional,

$$E_{\mathrm{X}\sigma}^{\mathrm{hybrid}} = a_{\mathrm{x}} E_{\mathrm{X}\sigma}^{\mathrm{HF}} + (1 - a_{\mathrm{x}}) E_{\mathrm{X}\sigma}^{\mathrm{GGA}}, \tag{2.14}$$

with a typically varying between 20 - 50%, depending on the functional used. $E_{\mathrm{X}}^{\mathrm{HF}}$ has the form

$$E_{\mathrm{X}}^{\mathrm{HF}} = -\frac{1}{2}\sum_{\sigma}\iint \phi_i^*(\mathbf{r})\phi_j^*(\mathbf{r}')\frac{1}{r_{12}}\phi_i(\mathbf{r})\phi_j(\mathbf{r}')d\mathbf{r}d\mathbf{r}' \tag{2.15}$$

and uses the occupied KS orbitals. One of the most common hybrid functionals is PBE0,[94] which has $a_x = 25\%$. Hybrid functionals address some of the shortcomings found within both pure HF and GGAs. They outperform both GGAs and HF by mitigating issues common in GGAs, such as delocalization error, and yet still include electron correlation absent in pure HF. However, as exact exchange is non-local in nature, hybrid functionals can become prohibitively expensive for large molecular systems and increasingly difficult with increasing unit-cell size for solid-state systems (becoming impractical for > 15 atoms/unit cell).

2.2 Periodic Boundary Conditions in the Solid State

The treatment of solids has a difficulty not seen within gas phase calculations, which is the requirement to treat an infinitely extending system with an infinitely large number of electrons. This is only surmountable due to the ability to break down solid-state systems into periodic components or unit cells. Unit cells are the most basic repeating structure of a given material from which the whole can be constructed. A unit cell provides a periodicity and can be completely specified by three Bravais lattice vectors:

$$\mathbf{R} = n_1\mathbf{a_1} + n_2\mathbf{a_2} + n_3\mathbf{a_3}, \tag{2.16}$$

where $\mathbf{a_1}$, $\mathbf{a_2}$, and $\mathbf{a_3}$ represent the primitive vectors which span the unit cell and n_1, n_2, and n_3 range through all integer values. As the entire repeating system can be represented by translations of the unit cell along the lattice vectors, the problem can be reduced from considering the whole infinitely repeating solid and its orbitals down to considering just the unit cell.

Given that the potential $U(\mathbf{r})$ can be represented using the periodicity of the Bravais lattice,

$$U(\mathbf{r}) = U(\mathbf{r} + \mathbf{R}), \tag{2.17}$$

Bloch's theorem[95] allows the eigenstates ψ of the one-electron Hamiltonian,

$$\hat{H} = -\frac{1}{2}\nabla^2 + U(\mathbf{r}), \tag{2.18}$$

to be chosen such that they have the periodicity of the Bravais lattice through the use of plane waves:

$$\psi_{n\mathbf{k}}(\mathbf{r}) = e^{i\mathbf{k}\cdot\mathbf{r}} u_{n\mathbf{k}}(\mathbf{r}), \tag{2.19}$$

with

$$u_{n\mathbf{k}}(\mathbf{r}) = u_{n\mathbf{k}}(\mathbf{r} + \mathbf{R}), \tag{2.20}$$

which can be written in the terms of its Fourier expansion as

$$u_{\mathbf{k}}(\mathbf{r}) = \sum_{\mathbf{G}} u_{\mathbf{k},\mathbf{G}} e^{i\mathbf{G}\cdot\mathbf{r}}. \tag{2.21}$$

Here, $\mathbf{k}$ is a reciprocal wave vector that satisfies $\mathbf{k} \cdot \mathbf{R} = 2\pi\delta_{ij}$, where δ_{ij} is the Kronecker delta. $\mathbf{G}$ can be any of the periodic wave vectors, such that $\mathbf{G} \cdot \mathbf{R} = 2\pi m$ for some integer m, where $\mathbf{R}$ is a lattice vector of the crystal. The electronic wavefunction can then be written as

$$\psi_i(\mathbf{r}) = \sum_{\mathbf{G}} c_{i,\mathbf{k}+\mathbf{G}} e^{i(\mathbf{k}+\mathbf{G})\cdot\mathbf{r}}. \tag{2.22}$$

This use of Bloch's theorem maps the problem of writing wavefunctions for an infinite number of electrons to one of expressing the wavefunctions in terms of a finite number of electrons, but using an infinite number of reciprocal-space vectors in the first Brillouin zone. This is then solved through the sampling of $\mathbf{k}$-space of the Brilloun zone.

In principle, $\mathbf{k}$-space must be sampled completely for an exact solution. In practice this can be avoided to give an accurate and tractable solution through an efficient sampling algorithm. Similar to the unit cell, as noted before, there exists a way to uniquely define a primitive cell in reciprocal or $\mathbf{k}$-space. The first Brillouin zone can be mapped by a set of $\mathbf{k}$-points, denoted as $x \times y \times z$, where every possible $\mathbf{k}$ in the infinite solid is equivalent to exactly one point in this region. There is an infinite density of $\mathbf{k}$-points within the first Brillouin zone and, therefore, an efficient yet accurate mapping must be used. One such scheme is that developed by Monkhorst and Pack,[96] which distributes the sampled $\mathbf{k}$-points homogeneously in columns and rows parallel to the reciprocal

lattice vectors and is based on point-group symmetries. Schemes like the Monkhorst-Pack scheme are viable even though they do not span all possible $\mathbf{k}$-points because they offer an efficient route to a sufficiently dense integration grid in reciprocal space, and a well-converged set of finite $\mathbf{k}$-points can still determine the total energy within an acceptable margin of error.

2.3 Planewaves and Pseudopotentials

A finite set of planewaves can be used as a basis because there are only discrete $\mathbf{G}$ vectors which fit within the lattice periodicity. The kinetic-energy cutoff that limits the energy/frequency of the planewaves is represented by

$$E^{\mathrm{cut}} = \frac{1}{2}|\mathbf{k} + \mathbf{G}_{\mathrm{max}}|^2, \tag{2.23}$$

which may be used in practice to limit the basis as the contributions of the higher Fourier components are ever diminishing. Separate kinetic-energy cutoffs are employed for the charge density and potential and for wavefunctions, respectively. As many planewaves are used to build up the true wavefunction, the calculation must be converged with respect to these cutoffs to ensure an accurate total energy.

In practice, even with the use of planewaves and efficient integration grids, there are caveats for calculations on solid-state systems. One such drawback is the inability of planewaves to easily describe wavefunctions containing sharp features, such as those at electron-nuclear cusps. To address this drawback and reduce the number of planewaves required to describe the wavefunctions and electron density, all atomic core regions are replaced with fixed pseudopotentials, so that the planewaves are only used to describe the valence charge density. These pseudopotentials have a simplified wavefunction with no nodes or cusps and, in case of norm-conserving pseudopotentials, a correct total charge. Outside some defined radial cutoff (r_{c}), the all-electron and pseudo wavefunctions are the same. Additionally, pseudopotentials can be classed as hard or soft, where a pseudopotential is considered soft when it requires a small number of planewaves for an accurate representation, and hard otherwise. The pseudopotentials also should be constructed from the specific type of exchange-correlation functional to be used in calculations.

Norm-conserving pseudopotentials are a specific type of pseudopotentials that allow for a basis set with a significantly lower cutoff for the highest Fourier mode of the planewaves. Norm-conserving pseudopotentials, first proposed in 1979 by Hamann, Schlüter, and Chiang[97] and later modified by Troullier and Martins,[98,99] follow four general conditions. The first is that the valence pseudo-wavefunction generated from the pseudopotential contains no nodes. Second, the normalized atomic radial pseudo-wavefunction with angular momentum l and the normalized radial

all-electron wavefunction are equal for a chosen cutoff radius, r_{cl}. Third, the charge within that cutoff region r_{cl} is equal for the pseudopotential (PP) and all-electron (AE) wavefunctions:

$$\int_0^{r_{cl}} \left|R_l^{\mathrm{PP}}(r)\right|^2 r^2 dr = \int_0^{r_{cl}} \left|R_l^{\mathrm{AE}}(r)\right|^2 r^2 dr. \tag{2.24}$$

Lastly, the valence pseudopotential and all-electron eigenvalues are also equal:

$$\varepsilon_l^{\mathrm{PP}} = \varepsilon_l^{\mathrm{AE}}. \tag{2.25}$$

Although, norm-conserving pseudopotentials have wide applications in solid-state calculations, they are not as accurate as the Projector Augmented-Wave (PAW) method developed by Blöchl in 1994 [100] and generalized by Kresse and Joubert. [101]

The PAW method is a type of augmented-wave method. Augmented-wave methods have various forms which began with the development of the augmented planewave method (APW). The APW method which aims to solve the Kohn-Sham equations, shown in matrix form as

$$\sum_{n'} (H_{n,n'} - \varepsilon_n S_{n,n'}) c_{n'} = 0, \tag{2.26}$$

where $H_{n,n'}$ is the Hamiltonian matrix,

$$H_{n,n'} = \left\langle \phi_n \right| -\nabla^2 + V_{\mathrm{eff}} \left| \phi_{n'} \right\rangle, \tag{2.27}$$

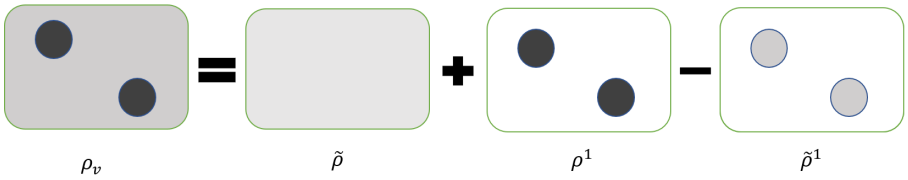
and $S_{n,n'}$ is the overlap matrix,

$$S_{n,n'} = \left\langle \phi_n | \phi_{n'} \right\rangle. \tag{2.28}$$

APW methods solve the Kohn-Sham equations 2.26 through linearising the eigenvalue problem and forms of this method are called linearised augmented planewave (LAPW) methods. [102,103] The LAPW method uses a dual basis type, where regions within the atomic spheres use atomic-like basis functions and the interstitial regions between atoms are treated with a planewave basis. The atomic regions are represented as muffin-tin spheres, where the number of planewaves required to represent the system is dependent on the muffin-tin cutoff radius, with a large region requiring fewer planewaves and a smaller requiring more planewaves. The LAPW method has the benefit of being a true all-electron method and therefore can give an accurate description of chemistry involving the atomic cores, but also can be quite costly, as the solving of the determinant of the matrix is non-trivial.

PAW is another common method of core-region reconstruction within solid-state calculations,

Figure 2.1: Schematic representation of PAW method. Figure adapted from Ref. 104.



which aims to have the accuracy seen within LAPW methods, with the efficiency seen with pseudopotential methods. This is achieved through transforming the true all-electron wavefunction, $\Psi(r)$, into a pseudised wavefunction, $\tilde{\Psi}(r)$, through the use of a transform operator:

$$\Psi(r) = \hat{T}\tilde{\Psi}(r). \tag{2.29}$$

This transform operator, $\hat{T}$, is written as $\hat{T} = 1 + \sum_R S_R$ and has some constraints so that the pseudo-wavefunctions remain smooth, so they can be expanded in terms of a minimal number of planewaves. S_R adds the difference between the all-electron and pseudo-wavefunctions, which is expanded in partial waves for free isolated atoms:

$$S_R|\tilde{\phi}_i\rangle = |\phi_i\rangle - |\tilde{\phi}_i\rangle, \tag{2.30}$$

where $|\tilde{\phi}_i\rangle$ is the pseudo partial wave and $|\phi_i\rangle$ is the all-electron valence partial wave. The augmentation region $\tilde{\Psi}_n(\mathbf{r})$ is then expanded in partial waves of $|\tilde{\phi}_i\rangle$ and is written as

$$\tilde{\Psi}_n(\mathbf{r}) = \sum_{i\varepsilon R} \tilde{\phi}_i(r) c_{in}, \tag{2.31}$$

where the c_i are determined by the projector functions $\langle\tilde{p}_i|$, which provide the contribution of each wave and is the projector part of PAW. This leaves the transform operator to be

$$\hat{T} = 1 + \sum_i \left(|\phi_i\rangle - |\tilde{\phi}_i\rangle\right) \langle\tilde{p}_i| \,, \tag{2.32}$$

and therefore the true wavefunction is recovered from $\Psi(\mathbf{r}) = \hat{T}\tilde{\Psi}(\mathbf{r})$. The PAW method is represented schematically in Fig. 2.1, where ρ_v is the total valence charge density, $\tilde{\rho}$ is the density from the pseudopotential calculation over the entire cell, ρ^1 represents the all-electron charge density within the PAW spheres, and $\tilde{\rho}^1$ the pseudo charge densities within the PAW spheres.[104] The PAW method achieves efficient and accurate densities by calculating the pseudopotential density and correcting the core region of each atom through the subtraction of the in-sphere pseudo

Table 2.1: Valence configuration and core-region cutoff radii, r_c, in atomic units for the B86bPBE PAW datasets used in this work.

Element	Valence Configuration		
	shell	occupation	r_c
H	1S	1.00	0.80
C	2S	2.00	1.00
	2P	2.00	0.90
N	2S	2.00	1.00
	2P	3.00	0.90
O	2S	2.00	1.00
	2P	4.00	0.90
Fe	4S	1.70	1.30
	2P	0.00	1.30
	3D	6.30	1.30
Ag	5S	1.50	2.20
	5P	0.00	2.20
	4D	9.50	1.70

part of the total charge density, replacing it with the all-electron in-sphere component.[104] This method has the benefit of retaining the core wavefunctions, with a reduction in the computational expense that arises from the planewave basis-set treatment of the core region.

All PAW datasets in this work were generated with B86bPBE using the "atomic" code from Quantum ESPRESSO,[105] version 5.1.1. The cutoff radii used for the pseudisation of the all-electron wavefunctions were set to those specified in Table 2.1. These components are important as PAW sphere overlap can cause spurious coulombic interactions between spheres.[104] This arises due to the unwanted augmentation of the charge densities. In this work, the possible minimum overlap distances are listed in Table 2.2. C−H bonds have the shortest bond lengths considered and also have one of the smallest differences between the optimized bond lengths and the sum of the core radii. The minimum distance between the PAW spheres is 0.23 bohr for C=O double bonds and this is the closest the spheres come to overlapping within the systems studied in this work. This is still beyond the range where the compensation densities would be expected to be overlapping and, therefore, PAW overlap would not be expected to be a major source of error within this work.

Table 2.2: Minimum bond distances from optimized geometries in this work, compared to the sum of maximum core cutoff radii for each element. All quantities are in atomic units.

Bond	Optimized Distance	$\sum r_c$	Difference
C-H	2.06	1.80	0.26
C-C	2.65	2.00	0.65
C-N	2.64	2.00	0.64
C-O	2.23	2.00	0.23
N-Fe	3.63	2.30	1.33
Fe-Ag	5.50	3.30	2.20
Fe-C	3.31	2.30	1.01
Ag-Ag	5.39	4.40	0.99

2.4 All-Electron Methods and Basis Sets

There exist two main approaches to treat the core region wavefunctions, one being pseudopotentials and the other being all-electron based methods. Although a pseudopotential-based method has the benefits of obtaining arbitrarily high accuracy with systematic increases in the kinetic-energy cutoffs for planewave basis sets and straightforward inclusion of scalar relativistic effects, they still have the drawbacks of transferability and the introduction of an approximation error. The alternative to the use of pseudopotentials is to treat all of the electrons in the core and valence on an equal footing by employing atom-centred basis sets. This allows for increased accuracy in calculations on excited states, electric and magnetic response properties, and high-pressure applications where a pseudopotential may either overlap with the valence wavefunction or not allow for a density change to occur.[63,64,106] Many types of atom-centred basis sets can be used both with pseudopotentials and in all-electron calculations. Specific focus in this section will be on the all-electron implementation of NAOs, with a survey of other common atom-centered basis sets.

The electronic wavefunction is expanded as a linear combination of the functions that comprise the basis set. Use of basis sets converts the three-dimensional partial differential equations from the base mathematical formalism in KS-DFT into algebraic equations, whose solution can be implemented on a computer. These basis functions can be either constructed from the atomic orbitals or planewaves, each of which have their own benefits and drawbacks. The KS orbitals can be written as linear combinations of basis functions, $\varphi_p(\mathbf{r})$, with optimized coefficients c_{ip}:

$$\phi_i(\mathbf{r}) = \sum_p c_{ip}\varphi_p(\mathbf{r}). \tag{2.33}$$

As mentioned previously, one major source of error in DFT calculations is the selection of the exchange-correlation energy functional. One of the next major sources of error can be found in the basis-set selection and its completeness. Basis set superposition error (BSSE) is a manifestation of the issues of basis set incompleteness. In practical quantum-chemical calculations, a finite basis must be used, as a complete basis would not be computationally tractable. The use of a finite basis means that, as subunits of the calculation (for example atoms, in atom-centred basis sets) are brought together, their basis functions begin to overlap. This allows for the subunits to borrow functions from the other nearby interacting components, which effectively increases its basis set. Thus, energies of molecular complexes are artificially lowered when compared to the separated molecules. While not used in this work, methods to address or minimize BSSE beyond the use of an ever-increasing basis set exist, such as the chemical Hamiltonian approach,[107,108] the traditional Boys-Bernardi counterpoise (CP) correction(which approximates the energy contribution arising due to this overlap and subtracts it from the energy),[109] and Grimme's geometric CP correction,[110–112] all of which aim to address BSSE in a systematic way but can themselves introduce error.

There are many different types of basis sets in common employ within computational chemistry codes. What follows is a list of the most common basis sets, along with their form and uses. As mentioned earlier, planewave basis sets are common within the solid state community. These basis sets have the form

$$\varphi_k(\mathbf{r}) = \mathrm{e}^{i\mathbf{k}\cdot\mathbf{r}}, \tag{2.34}$$

and are desirable for periodic systems, although they do have the caveat of requiring pseudopotentials, as mentioned in the section on planewave DFT above.

Slater-type orbitals (STOs) are an obvious first choice of atom-centered basis sets for electronic structure theory due to their exponential decay at long range and their nuclear cusp. These have the form

$$\varphi_{nlm}(\mathbf{r}) = Nr^{n-1}\mathrm{e}^{-\alpha r}Y_{lm}(\theta,\phi), \tag{2.35}$$

where n, l, and m are the quantum numbers, N is a normalization factor, α an adjustable exponent, and $Y_{lm}(\theta,\phi)$ are the spherical harmonics. STOs correctly capture the nature of the wavefunction within the nuclear cusp region,[113] although they are difficult to use in a computationally expedient manner due to the derivative discontinuity at the nuclei and integration of the radial part.[114,115]

In order to address these mathematical shortcomings, Gaussian-type orbitals (GTOs) were developed. While missing the nuclear cusp, these functions allow for easier treatment of the nuclear core regions and can be constructed of many primitive Gaussian functions to create a function that is analytically solvable/integrable but closely matches the form of the wavefunction.[114–117]

Gaussian-type orbitals have the form

$$\varphi_{nlm}(\mathbf{r}) = Nr^{n-1}\mathrm{e}^{-\alpha r^2}Y_{lm}(\theta,\phi), \tag{2.36}$$

which is comparable to the STO form, except for the power of r in the exponential. GTOs and STOs are both atom-centered and commonly used in all-electron calculations, although they can also be used in conjunction with pseudopotentials, as is common for heavy elements. GTOs have issues with their radial tails, which decay very slowly and require many primitive gaussians in order to correctly capture the true electronic wavefunction. This increases the computational expense and can lead to poor SCF convergence, which can make the choice of a Gaussian basis set unappealing for many periodic systems, although codes such as CRYSTAL[72] do employ GTOs for solid-state systems.

NAOs are another type of atom-centred, all-electron basis set, which allow for the treatment of periodic systems, but without the need of pseudopotentials to be computationally tractable.[63] NAOs have the form

$$\varphi_{nlm}(\mathbf{r}) = \frac{u(r)}{r}Y_{lm}(\theta,\phi). \tag{2.37}$$

NAOs generally treat the angular component $Y_{lm}(\theta,\phi)$ as an angular momentum function, the same as in GTOs and STOs.[63,106] The flexibility of NAOs comes in the form of the radial component, $u(r)$, which satisfies the single-particle, Schrödinger-like equation

$$\left[-\frac{1}{2}\frac{d^2}{dr^2} + \frac{l(l+1)}{r^2} + v_i(r) + v_{\mathrm{cut}}(r)\right]u_i(r) = \varepsilon_i u_i(r). \tag{2.38}$$

The form of the $v_i(r)$ term can correspond to Gaussian harmonic oscillators,[118] hydrogen-like potentials,[119–121] or free-atom or free-ion potentials,[119–122] as well as many other forms.[63,64] The key point is that these functions can be strictly localized by $v_{\mathrm{cut}}(r)$, which cuts off the slowly decaying tails, and provides functions that are strictly confined to a certain domain in space.[63,64] This allows for the expensive steps in the SCF procedure, such as integrations or density updates, to scale linearly with system size, which is the source of the NAO method's efficiency.[63,64,106]

As discussed earlier, integrals that involve the exchange-correlation functionals or potential cannot trivially be solved and require numerical methods to compute. Evalutation of the exchange-correlation energy requires numerical integration over a grid of points, with many pseudopotential codes acheiving this through the use of even-spaced grids. For chemical systems, the density changes rapidly near the atomic nuclei. Thus, an equally distributed grid of points in Cartesian space is highly inefficient for all-electron calculations, and would either require a massively large number of total points or miss fully characterizing the density changes. An alterative method must

then be sought and arises in the form of the grids proposed by Becke in 1988.[123]

In numerical integration, we must evaluate 3D molecular integrals of the form

$$I = \int F(\mathbf{r}) d\mathbf{r} \approx \sum_i A_i F(\mathbf{r}_i), \tag{2.39}$$

where $F(\mathbf{r})$ is an arbitrary integrand. These integrals can be approximated by the summation of the integrand over discrete integration points, $\mathbf{r}_i$, multiplied by their integration weights, A_i. Rather than spreading the points equally across the system of interest, it can be partitioned into atomic regions, where the numerical integration is carried out via spherical coordinates. This splitting of the function $F(\mathbf{r})$ is done through employing relative weight functions, $w_n(\mathbf{r}_i)$, which are assigned to each nucleus n in the system, sum to 1 within the vicinity of each atom, and decay to zero at all other nuclei:

$$\sum_n w_n(\mathbf{r}_i) = 1. \tag{2.40}$$

This then allows us to write

$$F(\mathbf{r}) = \sum_n F_n(\mathbf{r}) = \sum_n w_n(\mathbf{r}) F(\mathbf{r}), \tag{2.41}$$

where the arbitrary integrand is partitioned into atomic regions, allowing the initial integral I to be written as

$$I = \sum_n I_n = \sum_n \left(\int w_n(\mathbf{r}) F(\mathbf{r}) d\mathbf{r} \right). \tag{2.42}$$

The exact selection of the integration weights can vary, but most DFT codes use the "Becke weights", which arise from smoothed Voronoi polyhedra.[123] The selection of these weights, assuming that they are numerically well behaved, lets us write each atomic subintegration, I_n, as a single-centre integral in spherical coordinates as

$$I_n = \iiint_V w_n(\mathbf{r}) F(\mathbf{r}) r^2 \sin\theta dr d\theta d\phi. \tag{2.43}$$

Lebedev quadratures are utilized to carry out the angular integration and the radial integrations are mapped from $0 < r < \infty$ to the interval $-1 < x < 1$ used in standard Gaussian quadratures, via the transform

$$r = r_m \frac{1+x}{1-x}, \tag{2.44}$$

where r_m is taken as half the empirical Bragg-Slater radii[124] and corresponds to the midpoint of the integration interval.[123] Overall, this definition allows for more integration points to be concentrated

at the nucleus, with ever-decreasing amounts of points contained within the tail region, providing an accurate and systematic prescription for increasing numerical precision with atom-centred basis sets.[123]

2.5 The Exchange-Hole Dipole Moment Dispersion Model

The exchange-hole dipole moment (XDM) dispersion model, developed by Becke and Johnson,[19,62,74,125] overcomes the lack of dispersion within conventional DFT exchange-correlation functionals. This is achieved by a post-SCF correction to the base DFT energy of the form

$$E = E_{\text{base}} + E_{\text{disp}}, \tag{2.45}$$

where E_{base} contains only the semi-local and local effects. The dispersion energy within a periodic lattice is given by

$$E_{\text{disp}} = -\frac{1}{2}\sum_{n}\sum_{\mathbf{L}}\sum_{ij}\frac{C_{n,ij}f_n(R_{ij,\mathbf{L}})}{R_{ij,\mathbf{L}}}, \tag{2.46}$$

with $\mathbf{L}$ indicating the lattice vector, $C_{n,ij}$ the n-th order interatomic dispersion coefficients, and $f_n(R_{ij,\mathbf{L}})$ a damping function for the deactivation of the dispersion interaction at short ranges.[19] In practice, XDM truncates equation 2.46 at the $n = 10$ term.[19,62]

For the XDM model, the dispersion coefficients are determined from second-order perturbation theory.[19,21,62,126] The first three pairwise $C_{n,ij}$ dispersion coefficients between atoms i and j are

$$C_6^{ij} = \alpha_i\alpha_j\frac{\langle M_1^2\rangle_i\langle M_1^2\rangle_j}{\alpha_j\langle M_1^2\rangle_i + \alpha_i\langle M_1^2\rangle_j}, \tag{2.47}$$

$$C_8^{ij} = \frac{3}{2}\alpha_i\alpha_j\frac{\langle M_1^2\rangle_i\langle M_2^2\rangle_j + \langle M_2^2\rangle_i\langle M_1^2\rangle_j}{\alpha_j\langle M_1^2\rangle_i + \alpha_i\langle M_1^2\rangle_j}, \tag{2.48}$$

$$C_{10}^{ij} = \alpha_i\alpha_j\frac{2\langle M_1^2\rangle_i\langle M_3^2\rangle_j + 2\langle M_3^2\rangle_i\langle M_1^2\rangle_j + \frac{21}{5}\langle M_2^2\rangle_i\langle M_2^2\rangle_j}{\alpha_j\langle M_1^2\rangle_i + \alpha_i\langle M_1^2\rangle_j}, \tag{2.49}$$

where α_i is the atom-in-solid polarizability,

$$\alpha_i = \frac{V_i}{V_{i,\text{free}}}\alpha_{i,\text{free}}, \tag{2.50}$$

which is proportional to the ratio between the in-solid (V_i) and free ($V_{i,\text{free}}$) atomic volumes. $\langle M_l^2\rangle$ ($l = 1, 2, 3, \dots$) are the expectation values for the exchange-hole multipole moments. Although

equation 2.46 only includes pairwise contributions to the dispersion energy, electronic many-body effects are accounted for in the construction of the dispersion coefficients from the exchange hole, where the fully-interacting electron density is used.[19,21]

As can be seen in equations 2.47–2.49, the exchange-hole multipole moments are required for the formulation of the XDM dispersion coefficients. The expectation values for these multipole moments are

$$\left\langle M_l^2 \right\rangle_i = \int w_i(\mathbf{r})\rho_\sigma(\mathbf{r})[r^l - (r - d_{X\sigma})^l]^2 d\mathbf{r}, \tag{2.51}$$

where w_i are the weights used in the partitioning scheme for the density. For XDM this is achieved through Hirshfeld partitioning:[127,128]

$$w_i(\mathbf{r}) = \frac{\rho_{i,\mathrm{free}}}{\sum_j \rho_{j,\mathrm{free}}(\mathbf{r})}, \tag{2.52}$$

where $\rho_{i,\mathrm{free}}$ is the sphericalized free atomic density of atom i. The partitioning weights have a value of one near atom i and close to zero elsewhere.

In equation 2.51, the exchange-hole dipole,

$$d_{X\sigma}(\mathbf{r}) = \int \mathbf{r}' h_{X\sigma}(\mathbf{r}, \mathbf{r}') d\mathbf{r}' - \mathbf{r}, \tag{2.53}$$

can be calculated either exactly, which uses the occupied orbitals, or using the Becke-Roussel (BR) exchange-hole model.[19,92] In the solid-state, the BR model is employed to approximate the exchange-hole, $h_{X\sigma}$, due to the prohibitive computational cost associated with exact exchange.[74] The BR approach also has been shown to be in better agreement with reference data for molecular C_6 dispersion coefficients and binding energies, due to the fact that it models a localized exchange-hole. This is a better approximation to the full exchange-correlation hole than can be described by Hartree-Fock alone, as it captures some aspects of electron correlation by the assumption that the exchange-hole is localized to a region of atomic size.[19,125,129,130] The BR model hole relies on the (spin-dependent) electron density (ρ_σ), the density gradient ($\nabla\rho_\sigma$), Laplacian ($\nabla^2\rho_\sigma$), and the kinetic-energy density (τ_σ),[19,92] and hence is classified as a meta-GGA functional.

The BR exchange hole is modelled as an off-centre exponential function with the form Ae^{-ar}, which is centred at a distance b from the position of the reference electron.[19,125] There are three constraints for the BR model that uniquely determine the three parameters: the exponent (a), normalization (A), and displacement (b). These constraints are that the hole must be normalized to -1 electron, deplete to the spin density at the reference point, and have the same curvature as the

exact exchange hole at the reference point.[19] These constraints cause the normalization to be

$$A = -\frac{a^3}{8\pi}, \tag{2.54}$$

and the density to be

$$\rho_\sigma = \frac{a^3}{8\pi} e^{-ab}. \tag{2.55}$$

The exact exchange hole curvature is

$$Q_\sigma = \frac{1}{6}\left[\nabla^2\rho_\sigma - 2\tau_\sigma + \frac{1}{2}\frac{(\nabla\rho_\sigma)}{\rho_\sigma}\right], \tag{2.56}$$

which gives the curvature constraint the form of

$$Q_\sigma = \frac{\rho_\sigma}{6b}(a^2 b - 2a), \tag{2.57}$$

where the positive-definite kinetic-energy density τ_σ is

$$\tau_\sigma = \sum_i |\nabla\psi_{i,\sigma}|^2. \tag{2.58}$$

The values of a and b are fixed by solving the non-linear equations that arise from combining equations 2.55 and 2.56 for $x = ab$:

$$\frac{xe^{-2x/3}}{(x-2)} = \frac{2}{3}\pi^{2/3}\frac{\rho_\sigma^{5/3}}{Q_\sigma}, \tag{2.59}$$

which must be solved via the numerical Newton-Raphson method.[92,131] The exchange-hole dipole is $d_{X_\sigma} = b$, where b is calculated from the rearrangement of equation 2.55 and the valence spin density to give

$$b^3 = \frac{x^3 e^{-x}}{8\pi\rho_\sigma}, \tag{2.60}$$

with the added constraint that, in certain cases, non-physical values of the exchange-hole dipole moment can be obtained, which manifest as $b > r$. In these cases, $b > r$ is replaced with $b = r$ as a limiting value.[19,125]

The last key component for discussion of equation 2.46 is the inclusion of a damping-function (f_n). The perturbation-theory expansion of the dispersion energy is valid in the limit of large atomic separation, but a damping function is used to prevent a divergence of the dispersion energy at small internuclear distances and correct errors in the multipolar expansion.[19] XDM takes a novel approach to this issue: rather than requiring the dispersion energy to approach zero at small

separations, it instead requires the dispersion force to approach zero and the dispersion energy approach a constant, non-zero value.[19] This is consistent with the perturbation theory result for two hydrogen atoms at short interatomic separations.[132] The Becke-Johnson damping function used in XDM[19,133] is given by

$$f_n(R_{ij}) = \frac{R_{ij}^n}{R_{ij}^n + (a_1 R_{c,ij} + a_2)^n}. \tag{2.61}$$

$R_{c,ij}$ denotes the internuclear distance at which the multipolar expansion breaks down and the successive dispersion-energy terms become equal:

$$R_{c,ij} = \frac{1}{3}\left[\left(\frac{C_{8,ij}}{C_{6,ij}}\right)^{\frac{1}{2}} + \left(\frac{C_{10,ij}}{C_{6,ij}}\right)^{\frac{1}{4}} + \left(\frac{C_{10,ij}}{C_{8,ij}}\right)^{\frac{1}{2}}\right]. \tag{2.62}$$

The parameters a_1 and a_2 are fit through minimization of residual errors between the computed and reference binding energies for non-covalently bound dimers.[19] It is important to note that these parameters depend upon the density functional employed by the calculation, but are transferable to all elements.[19]

The contribution to the atomic forces and the stress tensor can be approximated from differentiating equation 2.46, under the assumption that the dispersion coefficients are approximately constant. For atom i, the force would be[74]

$$\mathbf{F}_{\mathrm{disp},i} = \sum_{\mathbf{L}} \sum_{j}{}' \sum_{n=6,8,10} \frac{n C_{n,ij} R_{ij\mathbf{L}}^{n-2}}{(R_{\mathrm{vdw},ij}^n + R_{ij\mathbf{L}}^2)^2} \mathbf{R}_{\mathbf{ijL}}, \tag{2.63}$$

and components of the stress tensor are represented by

$$\sigma_{\mathrm{disp},\xi\eta} = -\frac{1}{2V} \sum_{\mathbf{L}} \sum_{ij}{}' \sum_{n=6,8,10} \frac{n C_{n,ij} R_{ij\mathbf{L}}^{n-2} (R_{ij\mathbf{L}})_\xi (R_{ij\mathbf{L}})_\eta}{(R_{\mathrm{vdw},ij}^n + R_{ij\mathbf{L}}^n)^2}, \tag{2.64}$$

where the V is the cell volume and ξ, and η are two Cartesian coordinates of x, y, z. The assumption of constant dispersion coefficients, although not exact, does not drastically affect most geometry minimizations.[74] In practice, several iterations of geometry relaxations, each with fixed dispersion coefficients, are done in order to converge the dispersion coefficients and the structural geometry. This approach has been shown to result in the same geometry for solids as if the dispersion coefficients were recalculated at each step, while being more computationally efficient.[74]

The XDM model is implemented within the Quantum ESPRESSO code and, in conjunction with planewave basis sets, shown to provide good performance for studies of surface adsorption,[134] and properties of layered materials,[135,136] which are systems of interest within this work.

2.6 Alternative Post-SCF Dispersion Methods

There are a number of alternative dispersion-correction methods for DFT. These can be broken down into two categories, the first of which builds dispersion into the base exchange-correlation functional. The second, which will be the main focus of this work, is an *a posteriori* correction added to the self-consistent DFT energy, of which the exchange-hole dipole moment (XDM) model is one example. Of this second type, there are two other classes of dispersion corrections in common use, one being the Grimme D series (D2, D3, D4) and the other being the Tkatchenko-Scheffler (TS) and subsequent many-body dispersion (MBD) correction models. These two series of models differ from XDM in the way they arrive at the components of equation 2.46. These methods will now be discussed and compared with the XDM model.

2.6.1 The Grimme-D Series of Dispersion Models

Grimme and colleagues have introduced a series of dispersion corrections, which are add-ons to the standard Kohn-Sham density functionals.[31,137] The Grimme-D2 model[30] contains only the leading-order dispersion-energy term and the $C_{6,ij}$ heteroatomic dispersion coefficients are derived from the geometric mean of the homoatomic values:

$$C_6^{ij} = \sqrt{C_6^i C_6^j}. \tag{2.65}$$

The homoatomic dispersion coefficients are based on DFT/PBE0 calculations of atomic ionization potentials, I_p, and static dipole polarizabilities, α:

$$C_6^a = 0.05 N I_p^a \alpha^a, \tag{2.66}$$

where N is the maximum atomic number for the elements in each given row of the periodic table. The damping function used for Grimme-D2 is given by

$$f_{\mathrm{damp}}(R_{ij}) = \left[1 + e^{-d(R_{ij}/R_r - 1)}\right]^{-1}, \tag{2.67}$$

where R_{ij} is the interatomic distance and R_r is the sum of atomic van der Waals radii, treated as parameters for each element. The D2 model also employs a global scaling factor, s_6, which depends on the functional used and is determined by a least-squares minimization of interaction-energy errors for 40 noncovalently bound complexes.[30] D2 has since been improved through the reformulation of the dispersion coefficients, the inclusion of higher-order dispersion coefficients, the inclusion of three-body terms (Axilrod-Teller-Muto, ATM), and the use of the Becke-Johnson damping function, to give the D3 model.[31,32]

Instead of using an empirical basis for the formulation of the dispersion coefficients in D2, the D3 dispersion coefficients are derived from the Casimir-Polder formula:[31]

$$C_6^{\mathrm{AB}} = \frac{3}{\pi}\int_0^\infty \alpha^{\mathrm{A}}(i\omega)\alpha^{\mathrm{B}}(i\omega)d\omega, \tag{2.68}$$

where $\alpha(i\omega)$ is the averaged dipole polarizability at an imaginary frequency ($i\omega$), which may be computed by time-dependent DFT. In practice, the dispersion contributions are calculated not directly from equation 2.68, and therefore are not computed from the $\alpha(i\omega)$ values for free atoms. Instead they are computed for reference stable hydrides, which exist for every element in the periodic table except for the rare gases.[31] The C_6^{AB} coefficient can then be calculated using the stable hydrides $\mathrm{A}_m\mathrm{H}_n$ and $\mathrm{B}_k\mathrm{H}_l$ as reference molecules, with no contribution from the hydrogen:

$$C_6^{\mathrm{AB}} = \frac{3}{\pi}\int_0^\infty \frac{1}{m}\left[\alpha^{\mathrm{A}_m\mathrm{H}_n}(i\omega) - \frac{n}{2}\alpha^{\mathrm{H}_2}(i\omega)\right]\cdot\frac{1}{k}\left[\alpha^{\mathrm{B}_k\mathrm{H}_l}(i\omega) - \frac{l}{2}\alpha^{\mathrm{H}_2}(i\omega)\right]. \tag{2.69}$$

Here, $\alpha^{\mathrm{H}_2}(i\omega)$ is the polarizability of the dihydrogen molecule, m, k, n, l are stoichiometric factors, and $\alpha^{\mathrm{A}_m\mathrm{H}_n}(i\omega)$ and $\alpha^{\mathrm{B}_k\mathrm{H}_l}(i\omega)$ are the reference polarizabilities of the stable hydrides. This allows for the D3 C_6 coefficients to be dependent upon the atomic coordination number (CN), which is defined as

$$\mathrm{CN}^{\mathrm{A}} = \sum_{\mathrm{A}\neq\mathrm{B}}^{N}\left[1 + e^{-k_1(k_2(R_{\mathrm{A,cov}}+R_{\mathrm{B,cov}})/r_{\mathrm{AB}}-1)}\right]^{-1}, \tag{2.70}$$

where $R_{\mathrm{A,cov}}$ and $R_{\mathrm{B,cov}}$ are the scaled covalent single-bond radii for atoms A and B, and the k_1 and k_2 terms are scaling parameters fit for carbon atoms in common structures. The C_6 for any fractional coordination in a specific chemical environment may then be obtained by interpolation between a set of reference values, $C_{6,\mathrm{ref}}^{\mathrm{AB}}(\mathrm{CN}^{\mathrm{A}}, \mathrm{CN}^{\mathrm{B}})$, computed according to equation 2.69.

Early implementations of Grimme-D3 utilize the damping function of Wu and Yang as in D2.[19] Later implementations of D3 utilize the BJ damping function, detailed above in equation 2.61.[31,32] This has been shown to improve the results from the D3 model and is now the default in most applications.[31,32]

The higher-order C_8 coefficients are also included and computed in a recursive fashion via

$$C_8^{\mathrm{AB}} = 3C_6^{\mathrm{AB}}\sqrt{Q^{\mathrm{A}}Q^{\mathrm{B}}}, \tag{2.71}$$

where

$$Q^{\mathrm{A}} = s_{42}\sqrt{Z^A}\frac{\langle r^4\rangle^{\mathrm{A}}}{\langle r^2\rangle^{\mathrm{A}}} \tag{2.72}$$

is the effective charge for atom A. $\langle r^4\rangle$ and $\langle r^2\rangle$ are radial expectation values, which are computed

from geometrically averaged atomic densities, Z^A is the nuclear charge factor, and s_{42} is a scaling factor fit for noble-gas atoms.[31]

Grimme's D3 model also has the ability to include a three-body ATM dispersion term. This leading non-additive term is derived from third-order perturbation theory and, for three atoms ABC, is written as

$$E^{\mathrm{ABC}} = \frac{C_9^{\mathrm{ABC}}(3\cos\theta_a\cos\theta_b\cos\theta_c + 1)}{(R_{\mathrm{AB}}R_{\mathrm{BC}}R_{\mathrm{CA}})^3}, \tag{2.73}$$

with $\theta_{a,b,c}$ representing the internal angles of the triangle formed between atoms ABC, and C_9^{ABC} the triple-dipole dispersion coefficient,

$$C_9^{\mathrm{ABC}} = \frac{3}{\pi}\int_0^\infty \alpha^{\mathrm{A}}(i\omega)\alpha^{\mathrm{B}}(i\omega)\alpha^{\mathrm{C}}(i\omega)d\omega, \tag{2.74}$$

which is approximated as

$$C_9^{\mathrm{ABC}} \approx -\sqrt{C_6^{\mathrm{AB}}C_6^{\mathrm{AC}}C_6^{\mathrm{BC}}}. \tag{2.75}$$

The ATM term is similarly damped to remove non-physical effects that arise from the dispersion contributions at close range.[32,33]

Although the Grimme-D3 model addresses many of the issues found in D2, it is still fundamentally an advanced form of atom typing.[21] For many systems, D3 can be as accurate as XDM, but D3 falls short in some cases due to the fact that it is not dependent on the density and cannot respond to changing chemical environments. Some headway has been made in the formulation of D4, which is the newest iteration of the series, and includes an oxidation-state dependence but, at this time, has not been extensively tested for solids.[21,138]

2.6.2 The TS and MBD Methods

The final post-SCF dispersion methods discussed are the works pioneered by Tkatchenko and colleagues, in the form of TS[35,36,139] and MBD.[140,141] The TS scheme, much like the Grimme-D2 model, truncates the dispersion-energy expansion at the C_6 term and does not include any higher-order terms, such as C_8. The TS method begins with the Casimir-Polder formula for the free-atom C_6's, as in equation 2.68. In order to arrive at the C_6 terms for an atom inside a molecule or solid, the TS scheme utilizes a simple volume scaling,

$$C_{6,ii}^{\mathrm{eff}} = \left(\frac{V_i^{\mathrm{eff}}}{V_i^{\mathrm{free}}}\right)^2 C_{6,ii}^{\mathrm{free}}, \tag{2.76}$$

making use of the direct relation between polarizability and volume:

$$\frac{\alpha_i^{\text{eff}}}{\alpha_i^{\text{free}}} \propto \frac{V_i^{\text{eff}}}{V_i^{\text{free}}} = \left(\frac{\int r^3 w_i(\mathbf{r}) \rho(\mathbf{r}) d^3\mathbf{r}}{\int r^3 \rho_i^{\text{free}}(\mathbf{r}) d^3\mathbf{r}} \right), \tag{2.77}$$

where the $w_i(\mathbf{r})$ are the Hirshfeld partitioning weights, as detailed above in XDM.[62,127] From this, the effective coefficient $C_{6,ij}$ can be determined as

$$C_{6,ij} = \frac{2\alpha_i \alpha_j C_{6,ii} C_{6,jj}}{\alpha_j^2 C_{6,ii} + \alpha_i^2 C_{6,jj}}. \tag{2.78}$$

TS also uses a Fermi-type damping function of the form[35]

$$f_{\text{damp}}(R_{ij}, R_{ij}^0) = \left[1 + \mathrm{e}^{-d\left(R_{ij}/sR_{ij}^0 - 1\right)} \right]^{-1}, \tag{2.79}$$

where R_{ij}^0 is the sum of the van der Waal radii, and d and s are free parameters.

The TS method was improved upon through the inclusion of the long-range many-body terms, which are neglected in the formulation of the dispersion coefficients from simple volume scaling.[140,141] This method was given the label of many-body dispersion (MBD) and shows significant improvements over TS.[140,141] This was achieved through the self-consistent screening formalism (SCS), which models the non-additives in the polarizabilities and dispersion coefficients arising from interactions with distant atoms.[36,139] SCS treats the atoms as spherical quantum harmonic oscillators with Gaussian-type densities. The initial polarizabilities of the oscillators are first calculated via the TS method, then allowed to interact through the screened Coulomb potential,

$$V_{\text{SCS}}(R_{ij}) = \text{erf}\left(\frac{R_{ij}}{\sqrt{2}(\sigma_i + \sigma_j)} \right) \frac{1}{R_{ij}}, \tag{2.80}$$

with σ representing the width of the Gaussian density distribution. The resulting system of equations is then solved in a self-consistent manner, which provides the final densities and oscillation frequencies of the interacting oscillators. From this, the dispersion coefficients and atomic polarizabilities for MBD are calculated and the dispersion energy is evaluated as the difference between the energy for the isolated and interacting quantum harmonic oscillators (with the screened Coulomb potential). This improvement allowed MBD to attain comparable accuracy in solids to that found in XDM, although convergence issues are common for ionic solids.[21]

2.6.3 Non-Local van der Waals Functionals

As mentioned previously, there is an entirely different approach that can be taken within DFT to address the lack of non-local dispersion terms within the base functional. The van der Waals

functionals insert these terms directly into the exchange-correlation functional.[50] They are inserted through a non-local kernel, which acts as a response function packaged into the correlation energy of the E_{XC} term.[50] These functionals all have the general form

$$E_{\mathrm{C}}^{\mathrm{nl}} = \frac{1}{2} \iint \rho(\mathbf{r}) \Phi(\mathbf{r}, \mathbf{r}') \rho(\mathbf{r}') d\mathbf{r} d\mathbf{r}', \tag{2.81}$$

where ρ is the total electron density and Φ is the non local correlation kernel. There are many different approaches to how this kernel is formed and with what base functional it is paired. Two of the main categories are the VV functionals of Vydrov and Voorhis[52] and the vdW-DF functionals of Langreth and Lundquvist.[41,142]

The vdW functionals have various caveats, such as the level of empiricism, the computational expense of having the dispersion energy recalculated at each SCF step,[52] and the sensitivity to the choice of base functional.[50] Whilst some work well for intermolecular interactions, they are much more computationally expensive than the post-SCF corrections for large systems due to their poor scaling with system size.

CHAPTER 3

INTERPRETING SURFACE-ADSORPTION CHEMISTRY FROM STM IMAGES GENERATED VIA DISPERSION-CORRECTED DFT

Note: All experimental data included in this chapter were provided by Dr. Miriam DeJong and Prof. Sarah Burke, at the University of British Columbia. All DFT calculations were performed by the author.

3.1 Previous Work

Heterogeneous catalysis employs a catalyst that is a different phase from the reactants and/or products. It is an important tool for the chemical industry, as it allows for the efficient large-scale generation of easily separable chemical products without the need for a further step of specialized separation. Heterogeneous catalysis is estimated to be a part of almost 90% of industrial chemical processes world wide,[143,144] such as in the food, petrochemical, pharmaceutical, and automotive industries.[145–148]

A key step to further develop heterogeneous catalysts is understanding of the fundamental processes at work. Solid-state heterogeneous catalysis follows a process consisting of adsorption of reactant molecules to a surface, reaction, and then dissociation or desorption from the surface. Previous work by Burke and colleagues used supramolecular chemistry and a metal-organic process for self-assembly to make a novel active catalyst material.[149,150] The experimental focus of this early work was generation of atomically precise, self-assembled metal-organic Fe-terpyridine-phenyl-phenyl-terpyridine [4′,4′′′′-(1,4-11-Phenylene)bis(2,2′:6′,2′′-terpyridine), TPPT] complexes on an Ag(111) surface, which were characterized using low-temperature Scanning Tunnelling

Microscopy (STM).

In order to investigate the initial steps of heterogeneous catalysis, the adsorbed Fe-TPPT complexes were exposed to either of the gaseous reagents CO or C_2H_4. These reactants have applications in many industrial catalytic processes, such as those in the refining industry, or combustion within car exhausts, where the metal catalyst can activate C=C, C−H, and C−O bonds.[151] Experimental characterization was performed by STM, which allowed for the imaging of Fe-TPPT complexes on the surface, before and after exposure to the gaseous CO and C_2H_4 reagents. The imaging before and after exposure aided in understanding of the aforementioned adsorption process, which is a key step in heterogeneous catalysis. However, STM images alone can be challenging to interpret and assign to specific chemical species on the surface.[152,153] Here, we will use theory in order to provide a more rigorous structural assignment for the experimental results.

Computational modelling of surface adsorption can be done with density-functional theory (DFT). Previous work studying adsorption of benzene on noble-metal surfaces has demonstrated the importance of dispersion and sensitivity to the choice of dispersion correction.[12,134] The process of physisorption is dominated by weak, long-range noncovalent interactions, but has little impact on the electronic levels. A full treatment of these long-range effects is essential to accurately describe the physisorption geometries and energies. A key missing long-range effect within conventional DFT is an accurate treatment of London dispersion interactions, where non-dispersion-corrected functionals yield drastically underestimated adsorption energies relative to those seen in experiment.[134] Empirical dispersion models like D2, D3, and TS[154–156] can model these missing forces, but tend to overestimate dispersion binding to metal surfaces.[12,134] This overestimation occurs due to their dispersion coefficients, which are based on free-atom values, being too large for bulk metals. Conversely, the XDM and MBD models have been found to treat the process of surface adsorption accurately, since their dispersion coefficients have been formulated to vary with chemical environment and both show similar changes in C_6 going from a free metal atom to a metal surface or bulk.[134] Such a flexible treatment of dispersion is central to the accurate generation of computational STM results.

In this Chapter, we modelled surface adsorption of two common gaseous reactants, CO and C_2H_4, with a model of the Fe-TPPT heterogeneous catalyst on the Ag(111) surface. This was achieved through the use of dispersion-corrected DFT using the XDM dispersion model. For the DFT simulations, a truncated Fe-terpyridine (Fe-tpy) complex was selected in order to accurately recreate the active site of the complex, while reducing the molecular size to make the calculations feasible. From the DFT results, STM images were generated computationally for both prebonded and bonded complexes of CO/C_2H_4 with Fe-tpy on the surface. Excellent agreement has been

found between the experimental and theoretical results, allowing us to unambiguously assign structures.

3.2 Scanning Tunnelling Microscopy Theory

STM was developed in 1981 by Binnig and Rohrer and has become a key tool in the imaging of nanostructures at the atomic scale.[157,158] STM offers the possibility of direct real-space determination of 3D surface structures using a sharp single-atom tip to apply a voltage to a sample surface. The STM tip is brought towards the surface at a constant resistance and moved across it via a piezodrive, which consists of 3 independent piezoelectric transducers for each of the cartesian axis (x, y and z).[159] The mapping of the surface then comes via the weakly flowing current, I, which occurs due to the tunnelling of electrons through a vacuum between the tip and surface. The vacuum tunnelling resistance is measured as the tip is scanned, and the height adjusted to maintain a constant tunnelling resistance, which yields a contour map of the surface.[159] The experimental formalism comes from the Bardeen approach,[160] which uses time-dependent perturbation theory. The tunnelling current is given to first order by

$$I = \frac{2\pi e}{\hbar} \sum_{\mu,\nu} f(E_\mu)[1 - f(E_v + eV)]|M_{\mu\nu}|^2 \delta(E_\mu - E_\nu), \tag{3.1}$$

where $\hbar$ is the reduced Planck's constant, e is the electron charge, $f(E)$ is a Fermi function, V is the applied voltage, E_μ is the energy of the state ψ_μ without tunnelling, and $M_{\mu\nu}$ is the tunnelling matrix elements between the states ψ_μ of the probe and ψ_ν of the surface.[159]

This work utilizes DFT in order to generate STM plots, which are compared to those found via experiment. The DFT calculations rely on the Tersoff-Hamann approximation, where the current is taken to be proportional to the calculated density of states at the Fermi level,

$$I \approx V \rho_{loc}(\mathbf{r}, V), \tag{3.2}$$

where I is the current, and V is the bias voltage. ρ_{loc} is the local density of states at the Fermi-level E_F,

$$\rho_{loc}(\mathbf{r}, V) = \sum_{\mathbf{k},n}^{E_F - eV \to E_F} |\psi_{\mathbf{k},n}(\mathbf{r})|^2, \tag{3.3}$$

where the sum over the one-electron states that have energies between $E_F - eV$ and E_F.[161]

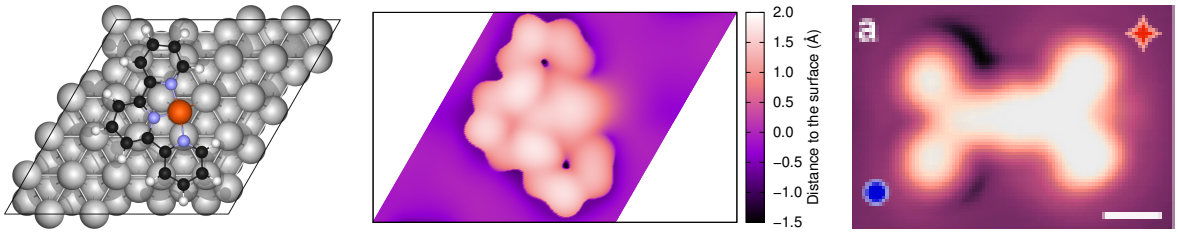
3.3 Computational Methods

This work utilized DFT in order to generate both theoretical STM plots and relative energy rankings for the possible catalytic species. Pseudopotential/plane-wave calculations were conducted using the projector-augmented-wave (PAW) method with Quantum ESPRESSO,[105] version 5.1.1.[162] All calculations employed the B86bPBE functional[17,18] with the XDM dispersion correction.[19,62,74,125] As discussed previously, the XDM model evaluates the dispersion energy as a sum over all atomic pairs, and is damped to prevent divergence at short internuclear separations. This damping function is controlled through two adjustable parameters based on the functional used. The value of the two adjustable parameters in the XDM damping function were set to their standard values of $a_1 = 0.6512$ and $a_2 = 1.4633$ Å.[19]

The Ag (111) surface was modelled as a 4-layer, 4×4 supercell with lattice constants fixed to their XDM-optimized values throughout this work. This model surface was selected as it has been previously shown to correctly capture the physisorption interaction between organic molecules and noble-metal surfaces when combined with XDM.[134] Next a truncated form of the Fe-TPPT complex was generated, consisting of Fe coordinated to a single terpyridine molecule (Fe-tpy), as shown in Fig. 3.1(a). Initial geometry relaxation was performed with the Fe-tpy placed on the Ag (111) surface and all surface atoms frozen. The planewave cutoffs for the kinetic energy and charge density were 50 and 400 Ry, respectively. These first calculations were done at the gamma point for both the singlet and triplet states of the Fe-tpy. For the triplet state, the initial spin bias was set to 2 and an unconstrained starting magnetization of 0.1 was placed on the Fe atom. Following this a second relaxation was performed, where the atomic positions of the Fe-tpy molecule and top two layers of the Ag (111) surface were allowed to relax. These calculations used an increased **k**-point grid of $2 \times 2 \times 1$, with the same planewave cutoffs for the kinetic energy and charge density. Finally, single-point energy calculations were conducted for evaluation of the adsorption energy. For the single-point energy calculations, a **k**-point mesh of $2 \times 2 \times 1$ and planewave cutoffs for the kinetic energy and charge density of 60 and 600 Ry were used, following previous work on molecular surface adsorption.[134]

Starting from the optimized Fe-tpy structure, two catalytically active reactants, carbon monoxide (CO) and ethylene (C_2H_4), were placed on the surface in a number of candidate configurations involving prebonding and bonding to the Fe-tpy complex to probe the energetic landscape and reflect the possible structures observed in the experimental STM images. Their geometries were then relaxed following the same computational protocol described above for the reactant-free Fe-tpy complex. These structures either collapsed to the prebonding and bonding configurations shown in Fig. 3.2 or were considerably higher in energy and not considered further. For all structures, except

Figure 3.1: Minimum-energy geometry of the Fe-terpyridine complex on the Ag(111) surface, along with the simulated STM image. The experimental image for the full Fe-TPPT complex is shown for comparison, adapted from Ref. 163.



(a) Fe-typ on Ag(111) (b) Simulated STM (c) Experimental STM

that of CO in the bonded configuration, both the triplet and singlet states were considered and the triplet found to be more stable. Supercell calculations were also undertaken on CO, C_2H_4, and triplet Fe-tpy at the gamma point, with cutoffs for the kinetic energy and charge density of 60 and 600 Ry, in order to evaluate the binding energies.

The STM images were generated using the CRITIC2 [161] code from the resultant densities from the single-point calculations with 1.2 times the number of occupied bands. CRITIC2 [161] uses the Tersoff-Hamann approximation, [159] where the modelled current, I, is proportional to the applied bias voltage and local density of states (LDOS) at the Fermi level. To generate the STM plots a sample bias of -0.02 eV was selected to match experiment.

3.4 Results and Discussion

3.4.1 STM Images

STM's ability to directly image reactive sites is a key tool in the understanding of experimental patterning of novel substrates on a surface. One key weakness for pure STM studies is the assignment of structures, where educated guesses can be made on what each image reflects but cannot be concluded with 100% accuracy. Here, we compare both experimental and theoretical STM results. As noted above, the experimental system consists of a Fe adatom coordinated to a single terpyridine (tpy) group of a terpyridine-phenyl-phenyl-terpyridine (TPPT) molecule adsorbed on an Ag (111) surface. The DFT calculations used a truncated Fe-tpy molecule, containing just the active site of the complex with a central Fe adatom coordinated to the terminal terpyridine (tpy) group, adsorbed on a 4-layer Ag (111) surface.

A schematic structural representation, as well as DFT-generated and experimental STM images are shown Fig. 3.1 for the Fe-tpy (or Fe-TPPT) complex, without any coordinated gaseous reactants. Fig. 3.1(a) is a schematic representation of the minimum-energy DFT structure. Both the singlet

and triplet configurations of the Fe-tpy were considered with the triplet yielding a lower binding energy (BE) by 5.9 kcal/mol. The DFT results place the z-distance of the Fe and the average of the rings at 2.34 and 3.2 Å respectively, above the surface, which is in line with the physisorption seen for organics on metal surfaces.[134]

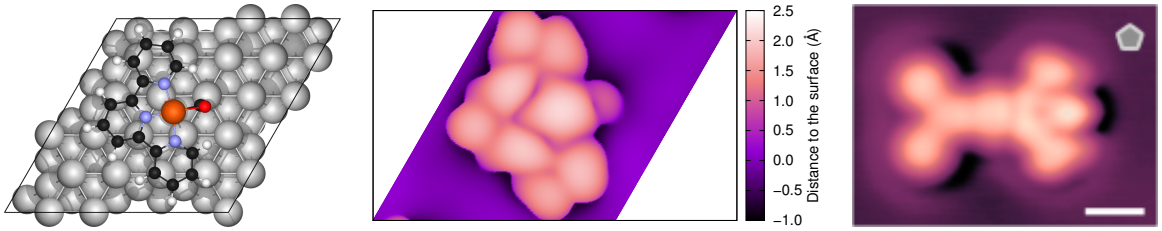
The experimental and simulated STM images for Fe-typ are compared in Fig. 3.1(b,c). In the experimental STM in Fig. 3.1(c), the iron is coordinated to the tpy on the right side of the TPPT molecule, as indicated by the orange diamond. The increased brightness upon iron coordination is due to the increased electron density on the negatively charged tpy ring. In both DFT and experimental STM images, the tpy bonded to the iron has a fairly uniform height, with the iron appearing less bright. This can be explained by both the partial positive charge on the Fe and the fact that, in the DFT structure, the Fe has a vertical height above the surface of 0.9 Å less than the average ring height.

The experimental focus of the work by Burke and colleagues was to use STM imaging to explore the reactivity of the active Fe sites when exposed to low concentrations of CO and C_2H_4. In the experimental results after CO exposure, two key motifs were observed. The first involves CO in a prebonded configuration, where it physisorbs to the Ag(111) surface, and the second motif corresponds to a bonded configuration, where the CO is fully coordinated to the metal centre through a metal-carbon bond. As the proportion the bonded species increased compared to the prebonded when annealed, the prebonded structure was determined to be a metastable surface-bound intermediate.[163]

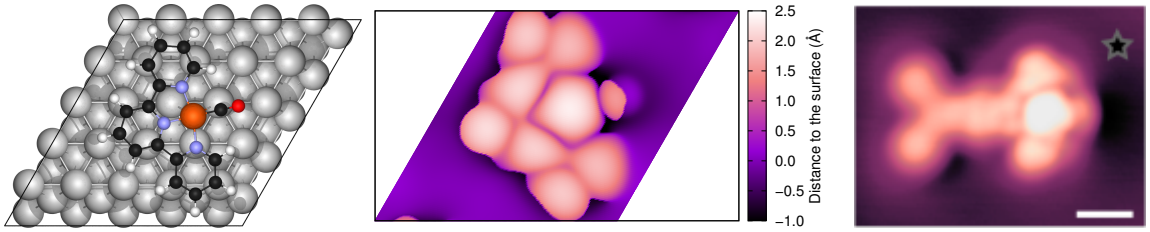
The DFT results for CO yielded only two minimum-energy motifs, seen in Fig. 3.2. All placements of the CO near the Fe would collapse to either the bonded or prebonded configuration (or some much higher energy state) depending on the choice of starting geometry. For the prebonded motif in Fig. 3.2(a), the CO is perpendicular to the surface and forms a C-Ag σ-bond, as well as a η^2 coordination to the Fe atom. For the bonding motif in Fig. 3.2(d), the CO is σ-bonded to the Fe through the carbon atom and lies parallel to the surface. The DFT calculations found that, in the prebonded configuration, the CO-Fe-tpy complex was most stable in the triplet state, consistent with the free Fe-tpy complex, whereas the CO-Fe-tpy complex is a singlet in the bonded configuration. This is likely due to the strong Fe$-$C$-$O-bond, which is stabilized by the back-bonding from the metal d-orbital to the π^* orbital of the CO that occurs in the bonded form of the complex. Back donation of electron density to the π system of the CO extends the C$-$O bond and shortens the metal-carbon bond. This phenomena changes the electronic state of the Fe centre to the singlet, instead of the triplet found for the CO prebonded or free Fe-tpy complexes.

The DFT-optimized geometries were then used to generate simulated STM images, as seen in

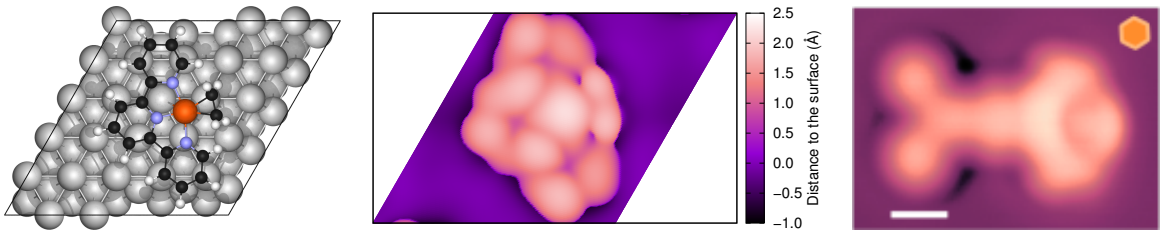
Figure 3.2: Low-energy structures of CO and C_2H_4 coordinated with the adsorbed Fe-tpy complex, along with the simulated STM image. The experimental images for the full Fe-TPPT complexes with the adsorbed species are shown for comparison, adapted from Ref. 163.



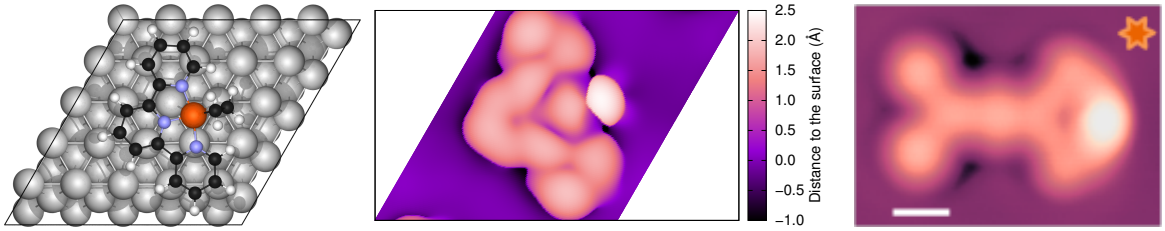
(a) CO prebonded (b) Simulated STM (c) Experimental STM



(d) CO bonded (e) Simulated STM (f) Experimental STM



(g) C_2H_4 prebonded (h) Simulated STM (i) Experimental STM



(j) C_2H_4 bonded (k) Simulated STM (l) Experimental STM

the middle column of Fig. 3.2. For the simulated STM of the bonded state in Fig. 3.2(e), the two parts of the CO molecule can be seen, with the carbon corresponding to the bright half sphere to the right of the Fe centre and a darker shadow behind it, which corresponds to the oxygen atom. When comparing the CO simulated and experimental STM images (Fig. 3.2(e-f)), both have the bright spot to the right of the Fe from the electron-rich carbon. Additionally, the central iron is much brighter and more prominent than in any other of the simulated or experimental STM images.

The simulated STM of the prebonded CO complex in Fig. 3.2(b) shows a single, slightly less-intense sphere to the right of the iron centre, which is the top of the CO oxygen. The simulated image also shows a region that appears to be below the surface as a black halo around the CO molecule. Although comparing the simulated and experimental STM images for the CO prebonded configuration, as in Figs. 3.2(b,c), provides a less convincing assignment, both do contain rounded features with a darkened halo to the right of the Fe centre. These consistent features and the prediction of only two low-energy motifs allowed for conclusive assignments of the experimental structures.

For C_2H_4, two key motifs were observed experimentally for direct interaction with the Fe-tpy complexes, which were again labelled as prebonded and bonded. The experimental work found that switching between the prebonded and bonded forms could be induced by a voltage pulse of -0.7 V for 200 ms and was entirely reversible.[163] The assignment of which is the prebonded versus the bonded configuration was based on the measurement of differential conductance by Scanning Tunnelling Spectroscopy (STS) localized around the Fe site, which would indicate a new Fe-centred state.[149,150] The bonded structure showed a new tunnelling resonance at -0.30 V, that was absent in the prebond species.[163] This indicated a downward shift of the Fe-centred state and a stabilization of the Fe-centred HOMO from the interaction with C_2H_4. Again via differential conductance measurements, the C_2H_4 prebonded configuration was found to be more stable than the CO prebonded configuration.[163]

The experimental STM images were compared to DFT results to further assign specific structures. As for CO, the C_2H_4 calculations either collapsed into one of two motifs, or were found to be much higher in energy. When investigating the two low-energy DFT motifs, the less-stable prebonded configuration in Fig. 3.2(g) was found to have the two carbons parallel to the Ag surface, whereas the carbons are perpendicular to the surface for the more-stable bonded configuration in Fig. 3.2(j). In the case of the prebonded motif, the iron centre lies 2.76 Å from the silver surface, which is significantly higher than in the bonded form, where the distance is 2.47 Å. Additionally, as for the bare Fe-tpy complex, the complex is most stable in the triplet state for both C_2H_4 motifs.

For the prebonded C_2H_4 configuration in Fig. 3.2(h), the simulated STM shows a rounded

Table 3.1: Binding Energies (BE) for the Fe-tpy species, along with the base-functional (BE_{base}) and XDM dispersion (BE_{disp}) contributions. Values for Fe-tpy are relative to the clean Ag(111) surface and isolated molecule. Values for CO and C_2H_4 are relative to the isolated molecules and the adsorbed Fe-tpy complex on the surface. All quantities are in kcal/mol.

Species	Configuration	BE	BE_{base}	BE_{disp}
Fe-tpy	–	78.3	21.3	57.0
CO	prebond	17.6	10.5	7.1
C_2H_4	prebond	19.9	8.1	11.8
C_2H_4	bond	26.4	14.7	11.7
CO	bond	48.6	42.0	6.6

termination with a uniform intensity to the right of the Fe centre, which corresponds to the C_2H_4 molecule as it associates with the iron. For the bonded configuration in Fig. 3.2(k), the simulated STM image has two distinct features. The first is an altered iron centre, which is triangular in shape with a reduced intensity similar to the rest of the Fe-tpy complex. The second is a much brighter lobe to the right of the Fe centre, which corresponds to the C_2H_4 molecule oriented perpendicular to the surface.

Unlike those for CO, the experimental and simulated STM images for C_2H_4 show clear similarities that allowed for straightforward assignments. The STM images for the prebonded motif in Fig. 3.2(h,i) share the key features of the low-intensity hemispherical lobes to the right of the Fe centre, arising from the C_2H_4 molecule parallel to the Ag surface. For the bonded configuration of C_2H_4 in Fig. 3.2(k,l), both STM images have a localized bright spot to the right of the Fe due to one ethylene CH_2 group that is pointed up, away from the Ag surface.

3.4.2 Binding Energies

The Fe-tpy complex adsorbs to the Ag(111) surface via a physisorption process. Due to this, accurate prediction of geometries and energies requires the inclusion of London dispersion interactions. This is illustrated in Table 3.1, which shows the binding energy of Fe-tpy on the surface, along with the decomposition into the base-functional and XDM contributions. In the case of Fe-tpy, dispersion accounts for 77% of the binding energy, illustrating the importance of its inclusion for these systems. Previous calculations for benzene adsorbed on an Ag(111) surface,[134] which employed the same methodology used here, gave a binding energy of 19.6 kcal/mol, coincidently in exact agreement with the reference experimental value.[164] That work also gave a binding energy of 18.7 kcal/mol for pyridine on Ag(111).[134] Our binding-energy result for Fe-tpy, which contains 3 pyridine rings, is slightly over 3 times higher than that for the single pyridine on Ag(111). The additional contribution to the binding energy comes from the dispersion interactions between the

Fe atom and the surface.

Table 3.1 also shows the binding energies for both CO and C_2H_4 with the adsorbed Fe-tpy complex, for both bonded and prebonded arrangements. Although reduced here, the dispersion contributions range from 13.6% to 60% of the total binding energies and are still important to the overall picture of reactant binding. The binding energies of the prebonded configurations for both CO and C_2H_4 are more sensitive to dispersion than their bonded counterparts are. The smallest dispersion contribution, of only 13.6%, is seen for the CO bonded species, which contains a direct Fe−C bond and has the highest overall binding energy of all four CO or C_2H_4 species discussed.

The DFT calculations for both CO and C_2H_4 found that the prebonded motifs were less stable than the bonded configurations, which confirmed our assignments of the STM results. The small binding-energy difference between the C_2H_4 prebonded and bonded configurations listed in Table 3.1 is consistent with the reversible conversion found in the STS experiments. For the cases of the CO motifs, the large binding-energy difference between the prebonded and bonded species in Table 3.1 is also consistent with the non-reversible conversion seen experimentally upon annealing. Another feature of the STS results that was recovered by the DFT binding energies is the fact that the CO prebonded complex was found to be less stable than the C_2H_4 prebonded complex. The inclusion of dispersion is key for this specific result, as the base-functional contribution alone (Table 3.1) would invert this ordering.

3.5 Conclusions

The ability of STM to image at the atomic level makes it a powerful tool for the fundamental understanding of surface chemistry. However, a major weakness of STM is that explicit assignment of the images to exact chemical species and subtle bonding arrangements can be extremely difficult. This work aimed to show DFT as a promising tool to aid in the assignment of STM images to specific species and bonding motifs, through the generation of high-quality physisorption geometries.

The calculations employed the B86bPBE functional[17,18] with the XDM dispersion correction[19,62,74,125] to study the physisorption of Fe-tpy, and its complexes with CO and C_2H_4, on an Ag(111) surface. The resulting binding energies and simulated STM images were then compared with the experimental work done by Burke and colleagues.[163] Previous work has shown that dispersion is important for predicting accurate geometries and energetics for the physisorption of organics on metal surfaces.[134] As theoretical STM plots are sensitive to geometry changes, we therefore expected the inclusion of dispersion to be key for the structural assignment between theory and experiment. The importance of including dispersion was also apparent in the energetic ordering as, without it, the relative stabilities of the CO and C_2H_4 prebonded complexes would be

switched and no longer reflect the trend seen in experiment.

Further experimental trends seen for the adsorption energies were also reflected within theory. The ability of CO to form a strong Fe – C bond made the structural assignment between prebonded and bonded complexes relatively simple. The large energetic difference agrees with the irreversible conversion to the bonded form seen experimentally after annealing. For the C_2H_4 complexes, it was not initially clear from experiment which structures would correspond to the bonded and prebonded motifs. Inspection of the DFT binding-energy results allowed assignment of the lower-energy structure as the bonded motif and the higher-energy as prebonded, and the calculated STM images had straightforward analogues with experiment. Confidence in the C_2H_4 result arose from the small difference in DFT adsorption energies, consistent with the observed reversibility of interconversion between the two motifs. Ultimately, the calculated binding energies, in addition to the generated STM images, made correct structural assignment of experimental results possible. The power of high-quality dispersion-corrected DFT calculations to aid interpretation of STM studies of surface chemistry can be seen from the results of this work.

CHAPTER 4

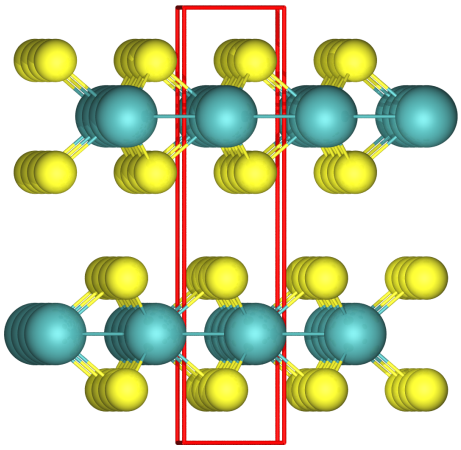
PROPOSAL

In the proposed work, a DFT-based tool will be developed for materials chemistry through combination of the linear-scaling FHIaims computational modelling code and the XDM dispersion correction. XDM will be implemented in FHIaims for use with GGA and hybrid functionals. The implementation will then be rigorously tested against common literature benchmarks, including the X23 set of molecular crystals and Bjorkman's set of layered materials, and the results compared to other state-of-the-art dispersion methods. The first aim of this work is to have the XDM module part of further distributions of the FHIaims code. Once a baseline for the accuracy of this tool has been developed we propose using it to further investigate the structure and properties of transition metal dichalcogenide (TMDC) heterojunctions. Such computational studies can guide experimental efforts to overcome the large contact resistance at TMDC-metal interfaces that currently prevents their use within production devices.

4.1 Transition Metal Dichalcogenides and their Interfaces

TMDCs are 2D layered materials of the form MX_2, where the M is a transition metal atom, such as Mo or W, and the X is from group 16. An extremely common example of a TMDC is that of MoS_2, as shown in Fig. 4.1, which exists in a trigonal prismatic 2H hexagonal structure. TMDCs are isostructural analogs of graphene, where the 2D layers are bound by weak van der Waals (vdW) forces, while the metal atoms are sandwiched between two chalcogenide layers through strong covalent bonds. TMDCs are a type of atomic semiconductors that have applications in the fields of electronics, batteries, catalysis, and tribology. Charge transfer in TMDCs has been shown to occur in-plane through the single layers and there exists a tunnelling barrier for charge transfer to occur between layers due to the weak vdW interactions and large interlayer spacing.[80] The band

Figure 4.1: Unit cell of molybdenum disulfide (MoS_2), a TMDC. MoS_2 is a 2D-material with the layers bound by vdW forces. Mo is represented as cyan and S as yellow, with the unit cell the red box. This is viewed along yz plane.



gap, which is important for device applications, can be controlled within a TMDC through the co-ordination environment of the metal, variations of the oxidation state of the metal atoms, and most importantly the material thickness/number of layers.[78,165]

The change in band gap with varying material thickness arises from the decreased interaction between the d-orbital of the metal with the anti-bonding p_z orbital of the chalcogen, which causes the band gap to increase as the number of layers is reduced.[165,166] MoS_2 shows this trend and has an indirect bandgap of 1.2 eV in the bulk and a direct bandgap of 1.85 eV in a monolayer.[165,167,168] Unlike graphene, TMDCs have both a desirable band gap and useful transport properties, such as carrier mobilities required for materials applications.[165,167,168] TMDCs have electron mobilities similar to that of Si, which is another factor that makes them a potential replacement for Si in semiconducting devices.[165,167,168]

One major application where the use of 2D-materials such as TMDCs have a promising future is in replacement of SiO_2 for channel materials in metal-oxide field effect transistors (MOSFETs), with the aim of extending Moore's law.[169] While TMDCs are a possible replacement for Si, a major issue with their implementation is the presence of a large contact resistance and the current rectifying effect that occurs between the TMDC and metal contact. The large contact resistance has the effect of drastically restraining the drain current achievable by the device.[170–173] Conventional bulk semiconductors have a top-contact arrangement, in which a metal such as Au, In, W, etc. will sit on top of SiO_2 and allow for a direct charge transfer to occur between metal and semiconductor. The low contact resistance occurs partially due to the ability of the metal to interact with the dangling bonds that exist after the cleaving of the bulk SiO_2. Conversely, TMDCs do not contain any dangling bonds and instead often form vdW contacts with the metal. Currently,

multilayered 2H-MoS_2 is the most widely used TMDC in devices and has been shown to have a contact resistance of approximately double that of SiO_2, with many other TMDC or 2D materials having even higher contact resistances of $3-4+$ times that of SiO_2.[82] As there is currently no easy method to lower contact resistance through doping, fundamental studies of metal-contact interfaces must be undertaken to offer possible avenues for low-resistance TMDC-based devices.

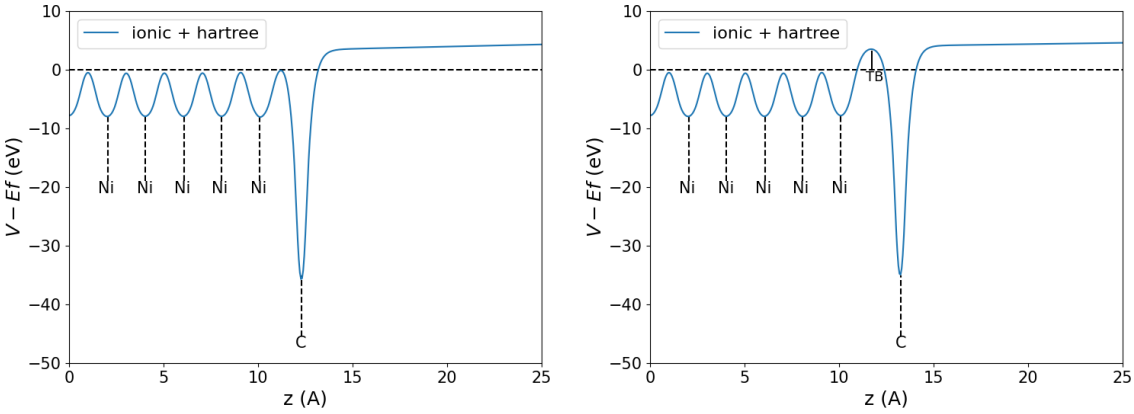
For metal-TMDC based devices, there are two main potential barriers that contribute to the resistance of the interface and deformation from an ideal ohmic contact. The first, being the Schottky barrier, is a potential energy barrier formed at the interface between a metal and a semiconductor. Upon first approximation, the Schottky barrier can be determined by the Schottky-Mott rule, where the Schottky barrier (ϕ_{SB}) is proportional to the difference between the metal's work function (ϕ_{metal}) and semiconductor-vacuum electron affinity (χ_{semi}):

$$\phi_{\mathrm{SB}} \approx \phi_{\mathrm{metal}} - \chi_{\mathrm{semi}}. \tag{4.1}$$

Schottky barriers arise due to the band bending that occurs when the semiconductor Fermi level lowers to meet the metal Fermi level. Interfaces with high Schottky barriers act as current rectifiers within a device, only allowing current flow in one direction. In practice, the size of the Schottky barrier is more complex than captured by the Schottky-Mott rule[174] as the type and form of chemical interactions between metal and semiconductor can allow for the formation of gap-states[175] within the semiconductor, pinning its Fermi level and altering the barrier height.[173] The other main potential barrier formed in metal-TMDC interfaces that contributes to contact resistance is a tunnelling barrier. A tunnelling barrier exists in these devices due to the vdW gaps between the metal and TMDC; this is another contributor to the contact resistance, and is highly dependent upon the metal-TMDC distance. The effect that proximity (in the z-direction) has on the (ionic plus Hartree) potential, V, can be seen for graphene on Ni, as in Fig. 4.2, and this figure shows the presence of a tunnelling barrier for the physisorbed contact. These two potential barriers are important for describing the carrier injection between the two materials and the ability to engineer an ohmic contact between a metal and a TMDC.[173]

There are three main types of interactions that can occur at metal-TMDC contact interfaces. The first, labelled Type-I, is a physisorbed contact, where there is little orbital overlap of the TMDC with the metal. Such contacts possess a large barrier to charge injection as there exists the normal Schottky barrier within the metal-SC interface, as well as an additional tunnelling barrier. Most top-contact metal-2D materials do not form covalent bonds and therefore fall into this category as a vdW gap is present. Although the vdW gap exists for many common metal and TMDC combinations, such as the Au-MoS_2 contact shown in Fig. 4.3(a), it does not occur in all cases.

Figure 4.2: Potential plots for graphene on a 6-layer Ni surface computed using B86bPBE-XDM with the Quantum ESPRESSO program. Geometries were taken from Ref. 135 and correspond to the top-fcc arrangement with a 2.47 Å lattice constant. All calculation parameters were chosen to match that work. (a) Chemisorbed graphene with no tunneling barrier, (b) Physisorbed graphene with a tunnelling barrier (TB) at the metal-graphene interface.



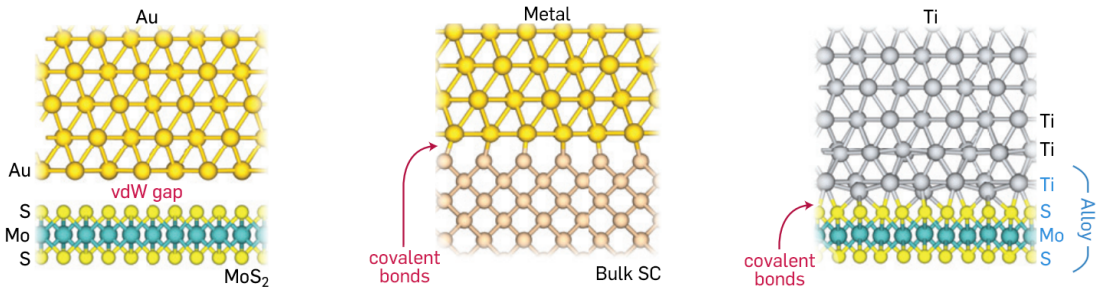
(a) Graphene chemisorbed on Ni.

(b) Graphene physisorbed on Ni.

An alternative is a chemisorbed bonding arrangement with the metal contact, labelled as type-II. Chemisorption is the preferred bonding arrangement in electrical devices as orbital overlap is maximized and there are negligible tunnelling and Schottky barriers to overcome. This is common in SiO_2-based devices with an Au contact.[82,173] Examples of metals that form covalent bonding arrangements with TMDCs are combinations such as Pd-MoS_2 and Ti-WSe_2. The last proposed metal-TMDC contact arrangement is one that involves an alloying or metallisation of the TMDC with the metal contact, which is labelled as Type-III. This metallised TMDC has the effect of eliminating the bandgap for the TMDC under the contact metal, creating a ohmic contact and a thinner Schottky barrier at the junction between the end of the metal and the TMDC not under the metal.[82,165] This third-type of contact interaction has been predicted via DFT to occur in Ti-MoS_2 interfaces.[82,173]

Current computational work in this area has primarily used density-functional models such as PBE-D2 and the LSDA.[82,165,173] For DFT, the probing of these interfaces can be computationally expensive. Past work for adsorbed graphene on metal surfaces uses a minimum of 6 metal layers to correctly model a bulk metal,[135,136] with other DFT studies of TMDC-metal interfaces utilizing a minimum of 6-7 layers.[82] Additionally, a large enough unit cell must be used to ensure a commensurate lattice between the metal and the TMDC. This can lead to unit cells on the order of hundreds of atoms to recreate reasonable lattice constants and minimize strain. Thus, a method must be selected to provide the highest accuracy with the lowest computational cost and scaling

Figure 4.3: Three types of common interface types for metal-semiconductor interfaces: (a) A Type-I interface showing the physisorption of MoS_2 onto Au with a vdW gap; (b) A Type-II interface containing strong orbital overlap, common in chemisorption of bulk semiconductor to a metal; and (c) A Type-III interface, where the TMDC has become metalized, illustrated for this case of MoS_2 on a Ti surface. This figure was reproduced from Ref. 173.



(a) Type I. (b) Type II. (c) Type III.

with system size. This can potentially be addressed through the use of NAOs and Becke grids, as mentioned earlier. Additionally, the DFT method used must capture the potential vdW forces between the metal and TMDC to correctly describe the interactions occurring within devices.

4.2 FHIaims Timings and Applications

The Fritz Haber Institute *ab initio* molecular simulations (FHIaims) package is a state-of-the-art electronic structure code designed for computational molecular and materials science. The FHIaims package is a NAO code that allows users to perform massively parallel computations for both finite molecules and periodic solids that scale linearly with system size.[63,64] These calculations can be performed with most modern density functionals, ranging from the LSDA to range-separated hybrids. FHIaims differs from many other modern periodic-solid codes, such as Quantum ESPRESSO, through the use of NAOs as basis functions, instead of plane-wave basis sets. Furthermore, the use of NAOs allows for the FHIaims package to be an all-electron code, avoiding the use of pseudopotentials. This provides the code with unique flexibility to probe systems where the inclusion of the core electrons would be necessary, or for systems where spin-orbit coupling is important, such as those containing heavy lanthanide and actinide elements. These aspects all make FHIaims an extremely appealing code for applications for TMDC interface design and understanding.

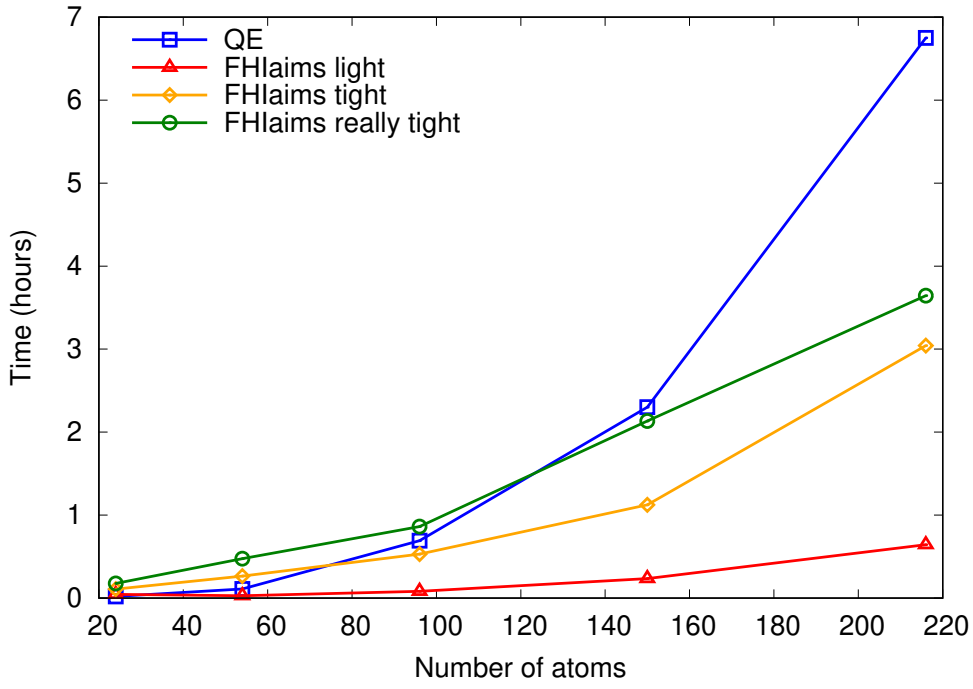
FHIaims achieves linear scaling through using NAOs as basis functions, employing efficient and switchable eigenvalue solvers, and alternative grid partitioning, such as radial shell methods

or adapted cut-plane methods.[63,64] These techniques are necessary as solution of the Kohn-Sham equations, a matrix eigenvalue problem, formally scales as $\mathcal{O}(N^3)$ with system size N. Other than the matrix eigenvalue problem, all other steps comprising a DFT calculation, such as the integration, density mixing, etc. scale approximately as $\mathcal{O}(N)$. A linear scaling is desirable as calculations on the proposed systems of TMDC heterostructures will quickly approach time and memory requirements that outstrip those available. The scaling efficiency can be seen in Fig 4.4 when comparing calculations using two current production codes: Quantum ESPRESSO and FHIaims.

In order to show the scaling performance for each of the codes, a series of single-point energy calculations were conducted for bulk MoS_2. Supercells of 2×2, 3×3, up to 6×6, were generated by repeating the unit cell in the x-y (in-plane) directions. The growth of the unit cells directly increases the system size, from 24 atoms in the 2×2 case up to 216 in the 6×6 case, which aids in indicating the scaling of each code. MoS_2 was selected as it is a common TMDC and will be one of the materials of interest. Calculations across both codes were run on the Graham Compute Canada heterogeneous cluster using 32 cores located on one node. All cores were located on Intel E5-2683 v4 Broadwell chips clocked at 2.1 Ghz. The PBE functional, with no dispersion correction, was used in all cases and a $4\times4\times1$ k-point mesh was used for all cell sizes. The Quantum ESPRESSO[105] calculations used the pseudopotential/plane-wave approach using the PAW method.[162] The single-point calculations were conducted using planewave kinetic energy cutoffs for the wavefunctions and charge density of 60 and 600 Ry, respectively. For the FHIaims calculations the "light", "tight", and "really tight" species defaults with the default tiers for basis sets were used. The FHIaims calculations used the atomic zora scalar relativistic correction, with all other settings assigned their default values within the code.

FHIaims builds up the basis sets for each atom in tiers, which contain the various radial functions (one for each of angular momentum s, p, d, etc.) and the type of those functions (hydrogenic or ionic). For example, the default "light" setting for Sulphur only contains basis functions from the first tier, $2p$(hydrogenic), $3s$(ionic), and $3d$(hydrogenic) basis functions, with the "tight" setting further adding some second tier functions, $4f$(hydrogenic), $4d$(hydrogenic), and $5g$(hydrogenic) basis functions. The default light basis sets, without any further tiers of basis functions, are considered numeric double-zeta plus polarization basis sets and increasing to the tight setting adds further polarization functions. Furthermore, without changing any other aspect of the calculation the basis sets can be arbitrarily increased within each of the light, tight and really tight defaults by adding more basis functions from higher tiers. In this way, the basis sets can be expanded to triple, quadruple, etc numeric basis sets (for Sulphur the addition of $1s$ and $4p$, for example)

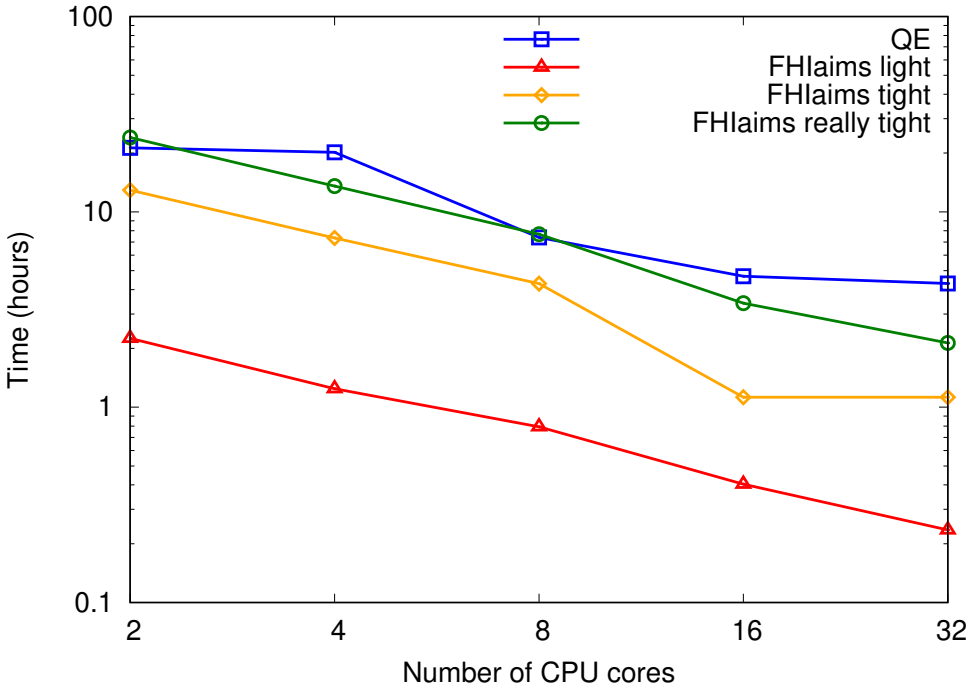
Figure 4.4: Wall time in hours taken for a single SCF energy evaluation for Quantum ESPRESSO and FHIaims using light, tight, and really tight species defaults, for MoS_2 cells of increasing size.



and by adding more polarization functions (for Sulphur the addition of $4f$ and $4d$, for example). The light, tight and really tight defaults further control all integration grids and the accuracy of the Hartree potential for the calculation. The light setting is recommended for pre-relaxations and structure searches. By default, it uses only the minimum recommended basis-set available in FHIaims, and its performance should be verified through comparison with larger basis sets. The tight setting is defined to provide meV-level converged energy differences. The really tight convergence retains the same default basis sets (including radial functions and cutoff radii) as for tight, but also over-converges the integration grids and Hartree potential.

It can be seen (in Fig. 4.4) that the PAW single-point calculations performed with Quantum ESPRESSO begin to scale poorly with system size and are less efficient on a per core basis for higher core counts. If this scaling trend continues for systems beyond $\sim$ 200 atoms (which is approximately 6.5 hrs), geometry relaxations, which require $\sim 20 - 100$ single-point energy calculations, will become intractable. When comparing single-point energy calculations between QE and FHIaims, even with the really tight settings, FHIaims is able to complete a single point calculation in under 3.6 hours (roughly a $2\times$ speed up) for a system of 216 atoms and the more gradual scaling will magnify this difference for larger systems.

Figure 4.5: Time in hours taken, represented logarithmically, for a single SCF energy evaluation using various numbers of CPUs. Results are shown for a 5×5 cell of bulk MoS_2 using Quantum ESPRESSO and FHIaims using light, tight, and really tight species defaults.



The SIESTA code is another electronic structure code that utilizes NAO basis sets and norm-conserving pseudopotentials and, like FHIaims, it has been demonstrated to scale as $\mathcal{O}(N)$ with system size.[70,176,177] While SIESTA already contains XDM dispersion,[178] there are a few fundamental issues barring its use for the proposed work. One key barrier to the use of SIESTA for TMDCs-metal heterojunctions is the availability of appropriately large basis sets for all elements. While double-zeta plus polarization (DZP) basis sets are available for most transition metals and chalcogens, they have been shown to systematically under bind layered materials,[178] and the larger triple-zeta plus polarization (TZP) basis sets are only available for C, H, N, and O.[70,176,177] Another major issue with SIESTA is the computational expense required to properly converge geometry relaxations. Previous works have shown that extremely tight convergence criteria are required in order to recover accurate relaxed geometries,[178,179] which can lead to 'endless' geometry optimizations.[176,178] This slow convergence of geometry relaxations leads to inefficient scaling when compared to other electronic structure codes. These factors, in addition to the overwhelming difference in the level of granular control, lead to the conclusion that FHIaims is a more promising alternative for accurate and computationally tractable study of TMDC heterojunctions.

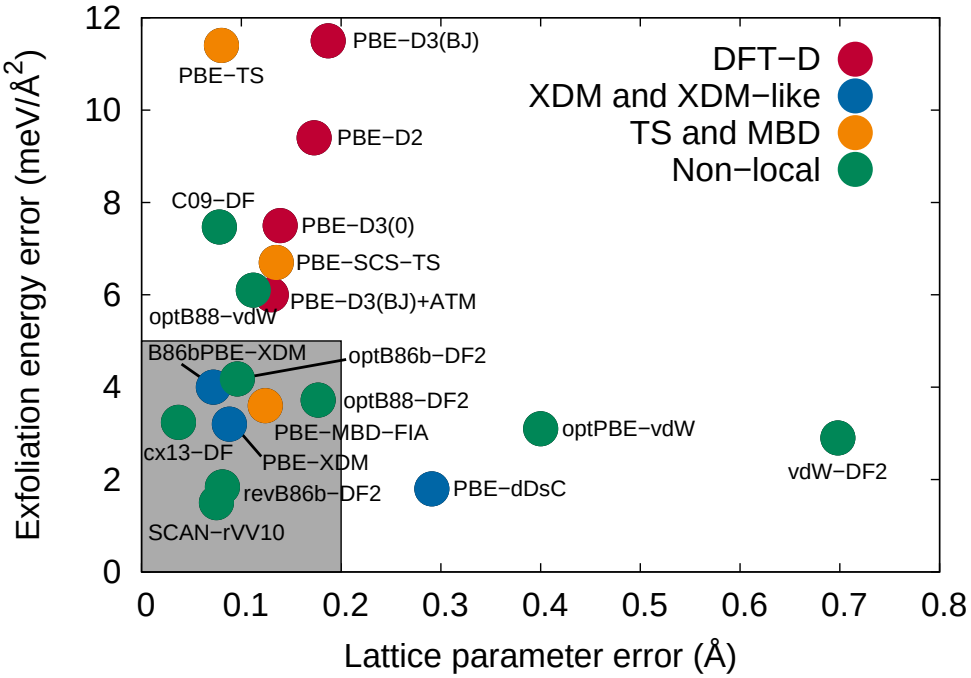
FHI-aims currently features Grimme's D-series, TS, and MBD dispersion corrections. However, as mentioned previously, these corrections are either less accurate or more computationally expensive than the XDM model. Thus, the implementation of the XDM model into the FHIaims package would be a highly desirable functionality for the investigation of interfaces of TMDCs for device applications.

4.3 Dispersion in Layered Solids

Correct characterization of dispersion forces is critical for accurate simulations of layered materials. The XDM model has the ability to respond to many differing chemical environments because the dispersion coefficients are non-empirical and depend directly on the electron density and related properties.[19] This flexibility is why XDM has been shown to be highly accurate for intermolecular complexes,[180] molecular crystals,[125] surface adsorption,[181] and layered materials.[74] The performance of XDM in solid-state applications has been shown to be class leading for common literature benchmarks, such as the X23 set of molecular-crystal lattice energies.[19,74,75] Although almost all DFT dispersion corrections, including those which are empirically derived, perform well for standard molecular dimer or crystal benchmarks, their accuracy can differ substantially for inorganic solids, such as layered materials or metal surfaces.

Notably, issues with empirical corrections can be seen for interlayer geometries and exfoliation energies of transition-metal dichalcogenides, as shown in Fig. 4.6.[76] Empirical dispersion correc-

Figure 4.6: Summary of dispersion-corrected DFT errors for Tawfik's benchmark of 11 layered materials;[76] the shaded box highlights an acceptable error range. Figure reproduced from Ref. 12.



tions such as Grimme's D-series of methods, and TS, generally achieve lattice parameters that match experiment, but systematically overbind TMDCs and yield incorrect exfoliation energies. This inaccuracy arises from the fact that the C_6 coefficients, in layered materials, differ greatly from both the free-atom values used in formulation of these methods, which can be seen in Table 4.1. XDM is the only method in Fig. 4.1 to predict the large reductions in homoatomic C_6 coefficients for layered materials relative to the free atoms.[12] The scaling of the C_6 coefficients with atomic volume used by the TS method is also unable to capture the changes in chemical environment needed to correctly model layered TMDCs.[12] Alternatively, certain functional combinations, such as optPBE-vdW, vdW-DF2 and PBE-dDsC, have been shown to correctly predict the exfoliation energies, but instead overestimate the equilibrium interlayer separations, as shown in Fig. 4.6.[12] The only dispersion corrections that are able to fully capture both the exfoliation energies and equilibrium geometries are the fractionally-ionic MBD method (MBD-FIA), certain non-local vdW functionals, and the XDM method, although the computational expense/time of these other methods is much greater than with XDM.[12,21]

XDM excels in its reproducibility across many systems of chemical interest, in addition to its computational expediency for systems of any size. Methods such as D2 and D3 provide the computational speed seen with XDM, but at the cost of reduced accuracy. Conversely, MBD-FIA

Table 4.1: Averaged C_6 dispersion coefficients in atomic units for the elements found in Tawfik's benchmark of 11 layered materials.[12,76] Table reproduced from Ref. 12.

atom	free	D2	D3	XDM
B	99.5	54.29	31.45	29.43
C	46.6	30.35	24.28	17.98
N	24.2	21.33	15.61	11.69
S	134.0	96.61	125.8	64.01
Se	210.0	219.2	210.5	98.01
Te	396.0	550.6	418.6	175.7
Mo	1029	427.9	337.1	365.8
Pd	157.5	427.9	265.9	112.9
Hf	1275	1409	421.0	562.8
Ta	1020	1409	458.8	399.7
W	847.9	1409	398.1	307.9

and non-local dispersion functionals can be accurate (if a good base functional is selected), but can be overly computationally expensive for heterojunctions. Ultimately, we need both an accurate and computationally expedient method in order to model TMDC interfaces; this leads to XDM being the rational choice for the systems of interest proposed in this work.

4.4 Proposed Work

4.4.1 XDM Implementation in FHIaims

The aim of this work is to implement both the B86b exchange functional and the XDM dispersion model in the FHI-aims software and test its performance for systems of interest. The combination of B86b exchange and XDM has been shown previously to provide the best accuracy for solids for a dispersion-corrected GGA.[180] XDM has been previously implemented in a number of codes such as Numol,[182] postg,[73,183,184] PSI4,[185] SIESTA,[176–178] and Quantum ESPRESSO.[74,105] Each of these codes has unique properties and applications: Numol is a fully numerical, grid-based all-electron code; postg utilizes the Gaussian[183] output files for gas-phase molecular calculations; PSI4 is an all-electron code also using Gaussian basis sets for molecular calculations; SIESTA is a numerical-orbital solid-state code;[178] and Quantum ESPRESSO is a planewave, pseudopotential solid-state code.[62,74,105] The SIESTA code will be utilized as a guide to implement XDM within FHIaims as it is also a numerical-orbital code. Many of the other codes listed above will serve as validation tools after the FHIaims XDM module has been written. The XDM implementation in FHIaims will allow for the computation of dispersion-energy corrections for any DFT method for single-point energy calculations. Following the implementation of XDM for single-point energy

calculations, force calculations and second-derivatives will be implemented for use in geometry relaxations and phonon vibrations.

The XDM dispersion module will be initially tested by evaluating the exchange-hole dipole moment from the BR model (see Eqn. 2.60) at radial grid points for both an isolated free atom and a free atom in a supercell. Argon will be used here as it is closed shell and isotropic, allowing for ease of testing and will follow the work for the implementation of XDM within SIESTA.[178] The results for the exchange-hole multipole moment integrals for the free argon atom will then be compared with the Numol, SIESTA, and Quantum ESPRESSO XDM results. Next, the FHIaims XDM implementation will need to be tested for consistency in the multipole moment integrals and polarizabilities for a select set of small molecules, such as H_2O, CO_2, CH_4, and for a set of simple solids such as diamond, graphite, and a crystal of urea. The results for small molecules will be compared against Gaussian and Psi4, and for the simple solids against SIESTA and Quantum ESPRESSO. The FHIaims implementation of these integrals will be made simpler as the Hirshfeld partitioning scheme used in XDM is already present within FHIaims.

XDM contains two parameters in the BJ damping function, which are key to its correct behaviour at small internuclear distances, and they must be parameterized for all density functionals and basis sets of interest. As FHIaims uses local basis functions, this makes exact (HF) exchange more practical than in planewave codes, so we will consider both the PBE and B86bPBE GGAs, as well as the hybrid-functionals PBE0 (25% exact exchange form of PBE),[186] B86bPBE-25X (25% exact exchange form of B86bPBE),[187] and HSE06.[188] The results will be compared with both the Quantum ESPRESSO[74,105] and the Gaussian/postg implementations.[73,183,184] As B86b exchange is not currently available in FHIaims, it will also have to be implemented. The current implementation of the PBE exchange functional within FHIaims, in addition to the implementation of the B86b exchange functional within Quantum ESPRESSO and SIESTA, will be used as guides for the implementation of B86b, due to the similarities between B86b and PBE exchange.

Basis-set selection is also an important component of the overall calculation accuracy. Basis-set superposition error is a particular issue for vdW complexes and can lead to an artificial lowering of energy and overbinding of the complexes.[110–112] A balance must therefore be struck between computational expediency and accuracy. The XDM damping function will be parametrized for a number of basis sets that are in common use with FHIaims. Previous FHIaims studies that used dispersion-corrected DFT utilized all of the common species defaults, from light through to really tight, with their default basis sets. For example, the crystal structure prediction work on molecular crystal polymorphs by Hoja and Tkatchenko utilized PBE+TS,[18] PBE+MBD,[18] and PBE0+MBD[186] functionals/dispersion combinations at the light settings (with the default basis

functions) for geometry optimizations and vibrational free energies, and at the tight level (again utilizing the default basis functions) for static lattice energies.[189] Work on metal-phthalocyanine (NiPc) dimers by Marom et al. utilized the PBE+TS functional/dispersion correction with the tier 2 NAOs (which would correspond with the default basis functions found in the tight settings) for geometry optimizations.[190] A further study benchmarking a wide range of functionals paired with the TS dispersion correction, as well as the semi-empirical Minnesota functionals (M06[57] and M06-L[56]), with FHIaims for the S22 set and other weakly bound systems used the tier 2 NAOs and showed similar convergence as with tier 3 and triple-zeta plus polarization basis sets.[191] Here, XDM will be parameterized for all commonly employed default basis sets from the light to really tight settings with the aforementioned GGA and hybrid functionals and comparison made to the Gaussian-basis results with postg program.[73,183,184] As is standard for XDM, the damping parameters will be fit by minimizing the root-mean-square percent error for the Kanneman-Becke 49 set of (KB49) set of intermolecular complexes, and then fixed.[19,74,178,180] The KB49 set includes complexes bound by dispersion, π-stacking, dipole-induced-dipole, dipole-dipole, and hydrogen-bonding interactions.[19,74,178,180] The S22 set of non-covalent complexes, which contains non-covalent interactions important within biological molecules,[192] is a subset of the KB49 set.

Due to the granularity of the control which FHIaims affords for selection of basis sets, integration grids, radial cutoffs, etc., the effect of each on the parameterization and performance of XDM will need to be investigated. Additionally, FHIaims can use mixed basis sets for different elements and this unique functionality (for a solid-state code) will be leveraged to aid in computational expediency and accuracy. Mixed basis sets have a history of use in gas-phase calculations, where they provide the ability to place more basis functions on the more electronegative elements, where they have the greatest effect on the energy, and less for those which are less electronegative. This increases the accuracy relative to a balanced small-basis calculation, while reducing the overall computational load relative to a balanced large-basis calculation. The ability to bias basis sets in this way is not available in other solid-state implementations of XDM and is one main advantage of the implementation and use of XDM within FHIaims.

After the damping function has been parameterized for various balanced and mixed basis sets, the XDM implementation will then be tested for the X23 set of molecular-crystal lattice energies and the results compared with other state-of-the-art dispersion methods. The X23 benchmark has been well tested with other implementations of XDM, so this will also be used to determine the overall performance of the FHIaims-XDM module.[19,74] Head-to-head testing for the X23 set will use a combination of functionals (PBE, B86bPBE), dispersion methods (TS, MBD, D3, XDM), and basis sets. Grimme's S12L set of large complexes[193] will be used as another benchmark

for the performance of FHIaims-XDM, as it is also common in the literature and will provide further verification. FHIaims-XDM will also be applied to the exfoliation of graphite, to test the implementation of the forces and efficiency of the geometry relaxations.[180,194] Lastly, the FHIaims-XDM module will be applied to TMDCs, using both Tawfik's set of 11 layered materials[76] and the full Bjorkman set of 26 layered materials.[77] Here, mixed basis sets will be optimized for a balance of accuracy and speed for the Bjorkman set and carried forward as a starting point for studies of TMDC heterojunctions. Head-to-head testing for the interlayer distances and exfoliation energies will be performed for a selection of functionals and dispersion methods (neglecting MBD due to convergence issues for these systems of interest).[76] These benchmark calculations will allow us to assess the performance of the FHIaims implementation of XDM compared to other codes for a wide range of systems, as well as the specific application of TMDCs. Upon final verification of the XDM module's performance, the aim will be to include it within future releases of the FHIaims code. This will add a well tested and accurate tool for the study of large (>200 atoms) and complex systems containing dispersion interactions.

4.4.2 Application to TMDC Interfaces

The ultimate aim for the development of FHIaims-XDM module is to apply this tool to study large TMDC-containing systems, such as heterojunctions or hybrid interfaces. This research is an important endeavour as the use of silicon in devices has begun to reach its useful limit. Alternative materials, such as TMDCs, may provide a potential future for the transistor devices by replacing Si as the semiconducting component of a transistor. Systematic studies of various metal contacts with TMDC surfaces will be critical in the realization of these devices from design to production. DFT studies of metal/TMDC interfaces will allow investigation of how the contact configuration, orientation, and bonding affect their contact resistance in a way which previously has been inaccessible.

In this work we aim to extend and improve upon previous DFT studies of TMDC-metal interfaces. DFT studies of TMDC heterostructures have almost always either used no dispersion correction, by employing the error-cancellation effects of the LDA or PW91, or used the PBE functional in conjunction with either the D3 or TS dispersion corrections.[82,173,195] Notably, Kang and colleagues[82] systematically investigated metal/TMDC contacts using In, Ti, Au, Pd, Mo, and W metals as contacts, and MoS_2 and WSe_2 as the selected TMDC monolayers. Three orientations of metal/TMDC interfaces were considered: a traditional top contact, a side contact, and a combined top and side contact. The TMDCs were found to posses different carrier mobilities based on the type of interface formed (Types I-III as referred above), as well as the orientation of the contact. Kang et al.'s work utilized the LDA functional with the D2 dispersion correction,[82] which recovered

the experimental band gap expected for the TMDCs. However, the use of the LDA functional with a dispersion correction will almost certainly overbind these interfaces, due to the additive effect between the LDA base functional's spurious overbinding and D2's dispersion binding. This could lead to underestimation of the tunnelling barrier in Type-I interfaces, as well as incorrect prediction of Type-II or III interfaces vs Type-I in some cases. These systems are a promising place to begin the study of metal-TMDC heterojunctions. Additionally, with the combined power of FHIaims with XDM, this body of work could be expanded on with a larger set of possible TMDCs, such as $MoSe_2$, WSe_2, and $MoTe_2$. We believe that this leaves further room to extend the field through the use of the XDM dispersion model with the FHIaims code.

Another factor that can cause issues for TMDC based devices is the strain that can be imposed due to lattice mismatch, or surface roughness, between the metal and TMDC contacts. Strain is an issue within TMDC interfaces; for example, in a pyrolytic graphite/monolayer MoS_2 interface, as little as a 2% strain can change the band gap from direct to indirect and reduce this gap by 4 eV.[79] Although strain has generally been understood to have a deleterious affect on TMDC device characteristics, some experimental work has been done in order to make use of the change in electronic and optical processes of TMDCs when under strain, for use in optoelectronics. Work by Wu, et al.[196] investigated the effect that strain had on the separation/transportation of photogenerated carriers and found that there was a $26\times$ improvement in photoresponsivity for metal-monolayer/MoS_2 phototransitors when under -0.36% compressive strain. As strain can be both a desirable and undesirable quality and can arise naturally depending on the application, a systematic computational study would be an effective tool in order to measure the effect that strain has on the electronic properties of metal-TMDC interfaces. Computational work by Saidi[197] investigated the effect that strain has on metal/MoS_2 heterostructures for Pd(111) and Pt(111) using PBE paired with the TS dispersion correction. The deformation of the metal surface under compressive and tensile strain was computed, varying the number of layers.[197] Saidi found that there was not a consistent behaviour across metals and, therefore, a systematic review for each metal and TMDC combination would be necessary in order to investigate the effects that varying strain and layer number would have for metal/TMDC interfaces. As strain is an important component to the TMDC bandgap, and therefore device performance, we propose a systematic study investigating the effect of strain, both compressive or tensile, for all noble metal-TMDC interface combinations.

Lastly, another proposed application of XDM in FHIaims is the investigation of metal/electride/TMDC heterostructures. Electrides are a class of ionic materials, where the anionic species is a localized electron.[198,199] The first electrides discovered were organic electrides, synthesized by Dye in 1974.[198,199] Since their initial discovery, there has been an ever growing number of

electrides proposed and synthesized, with the first 2D-electride, $[Ca_2N]^+e^-$, being discovered in 2013.[198–200] $[Ca_2N]^+e^-$ consists of layers of $[Ca_2N]^+$ cations, separated by regions of interstitial electron density.[199,200] Electrides have attracted attention in recent years due to their ability to readily donate electrons to surrounding materials. In this way, $[Ca_2N]^+e^-$ could serve as a possible intermediate layer between a metal and TMDC, due to its ability to modify the electronic properties of neighbouring materials.[199,201] Current ongoing work has focused on this property of $[Ca_2N]^+e^-$ to inject electrons into a MoS_2 layer, and overcome the tunnelling barrier, which is present due to the vdW gap.[202] However, due to the computational expense, this work has been limited to the Ca_2N/MoS_2 interface, and neglects any additional metal layer. We propose that FHIaims-XDM will allow for feasible studies of device stacks containing metal/electride/TMDC interfaces. We will aim to investigate the metals In, Ti, Au, Pd, Mo, and W as contacts, $[Ca_2N]^+e^-$ as our electride layer, and MoS_2, WS_2 WSe_2,$MoSe_2$, WSe_2, and $MoTe_2$ as possible TMDCs, with the goal of identifying optimal combinations that minimize the effect of the tunnelling barrier within these interfaces.

Once the XDM module is integrated within FHIaims, the study of common heterojunctions within transistors can be feasibly be investigated. Ultimately, the implementation of XDM within the FHIaims code will provide a new computational tool to enable novel science far beyond the scope of what is proposed here.

BIBLIOGRAPHY

[1] Becke, A. D. Perspective: Fifty Years of Density-Functional Theory in Chemical Physics. *J. Chem. Phys.* **2014**, *140*, 18A301.

[2] Burke, K. Perspective on Density Functional Theory. *J. Chem. Phys.* **2012**, *136*, 150901.

[3] Hohenberg, P.; Kohn, W. Inhomogeneous Electron Gas. *Phys. Rev.* **1964**, *136*, B864–B871.

[4] Kohn, W.; Sham, L. J. Self-Consistent Equations Including Exchange and Correlation Effects. *Phys. Rev.* **1965**, *140*, A1133–A1138.

[5] Sherrill, C. D. Frontiers in Electronic Structure Theory. *J. Chem. Phys.* **2010**, *132*, 110902.

[6] Casely, I. J.; Ziller, J. W.; Fang, M.; Furche, F.; Evans, W. J. Facile Bismuth-Oxygen Bond Cleavage, C-H Activation, and Formation of a Monodentate Carbon-Bound Oxyaryl Dianion,$(C_6H_2tBu_2-3,5-O-4)^{2-}$. *J. Am. Chem. Soc.* **2011**, *133*, 5244–5247.

[7] Mo, Y.; Ong, S. P.; Ceder, G. First-Principles Study of the Oxygen Evolution Reaction of Lithium Peroxide in the Lithium-air Battery. *Phys. Rev. B* **2011**, *84*, 205446.

[8] London, F. On the Theory and Systematic of Molecular Forces. *Z. Phys.* **1930**, *63*, 245–279.

[9] Stone, A. *The Theory of Intermolecular Forces*; oUP oxford, 2013.

[10] Kolar, M.; Kubar, T.; Hobza, P. On the role of London dispersion forces in biomolecular structure determination. *J. Phys. Chem. B* **2011**, *115*, 8038–8046.

[11] Chapman, C.; Ting, E. C.; Kereszti, A.; Paci, I. Self-Assembly of Cysteine Dimers at the Gold Surface: A Computational Study of Competing Interactions. *J. Phys. Chem. C* **2013**, *117*, 19426–19435.

[12] Otero-de-la-Roza, A.; LeBlanc, L. M.; Johnson, E. R. Pairwise Dispersion Corrections Can Describe Layered Materials Accurately. *J. Phys. Chem. Lett.* **2020**, *11*, 2298–2302.

[13] Liu, W.; Tkatchenko, A.; Scheffler, M. Modeling Adsorption and Reactions of Organic Molecules at Metal Surfaces. *Acc. Chem. Res.* **2014**, *47*, 3369–3377.

[14] Micoulaut, M.; Piarristeguy, A.; Flores-Ruiz, H.; Pradel, A. Towards Accurate Models for Amorphous GeTe: Crucial Effect of Dispersive van der Waals Corrections on the Structural Properties Involved in the Phase-change Mechanism. *Phys. Rev. B* **2017**, *96*, 184204.

[15] Moellmann, J.; Grimme, S. Importance of London Dispersion Effects for the Packing of Molecular Crystals: A Case Study for Intramolecular Stacking in A Bisthiophene Derivative. *Phys. Chem. Chem. Phys.* **2010**, *12*, 8500–8504.

[16] Otero-de-la-Roza, A.; DiLabio, G. *Non-Covalent Interactions in Quantum Chemistry and Physics*; Elsevier: Amsterdam, Netherlands, 2017.

[17] Becke, A. D. On the Large-Gradient Behavior of the Density Functional Exchange Energy. *J. Chem. Phys.* **1986**, *85*, 7184–7187.

[18] Perdew, J. P.; Burke, K.; Ernzerhof, M. Generalized Gradient Approximation Made Simple. *Phys. Rev. Lett.* **1996**, *77*, 3865–3868.

[19] Johnson, E. R. In *Non-covalent Interactions in Quantum Chemistry and Physics*; Otero-de-la-Roza, A., DiLabio, G. A., Eds.; Elsevier, 2017; Chapter 5, pp 169–194.

[20] Zacharia, R.; Ulbricht, H.; Hertel, T. Interlayer Cohesive Energy of Graphite from Thermal Desorption of Polyaromatic Hydrocarbons. *Phys. Rev. B* **2004**, *69*, 155406.

[21] Otero-de-la Roza, A.; LeBlanc, L. M.; Johnson, E. R. What Is "Many-Body" Dispersion and Should I Worry About It? *Phys. Chem. Chem. Phys.* **2020**, *22*, 8266–8276.

[22] Salem, L. The Calculation of Dispersion Forces. *Mol. Phys.* **1960**, *3*, 441–452.

[23] Dalgarno, A.; Davison, W. D. *Advances in Atomic and Molecular Physics*; Elsevier, 1966; Vol. 2; pp 1–32.

[24] Atkins, P. W.; Friedman, R. S. *Molecular Quantum Mechanics*; Oxford university press, 2011; Chapter 4, pp 414–417.

[25] Unsöld, A. Quantentheorie des Wasserstoffmolekülions und der Born-Landéschen Abstoßungskräfte. *Z. Phys.* **1927**, *43*, 563–574.

[26] Jones, J. E. On the Determination of Molecular Fields.—II. From the Equation of State of a Gas. *Proc. R. Soc. Lond.* **1924**, *106*, 463–477.

[27] Vanommeslaeghe, K.; Hatcher, E.; Acharya, C.; Kundu, S.; Zhong, S.; Shim, J.; Darian, E.; Guvench, O.; Lopes, P.; Vorobyov, I.; MacKerell Jr., A. D. CHARMM General Force Field: A Force Field for Drug-like Molecules Compatible with the CHARMM All-Atom Additive Biological Force Fields. *J. Comput. Chem.* **2010**, *31*, 671–690.

[28] Wang, J.; Wolf, R. M.; Caldwell, J. W.; Kollman, P. A.; Case, D. A. Development and Testing of a General Amber Force Field. *J. Comput. Chem.* **2004**, *25*, 1157–1174.

[29] Jorgensen, W. L.; Tirado-Rives, J. Potential Energy Functions for Atomic-Level Simulations of Water and Organic and Biomolecular Systems. *Proc. Natl. Acad. Sci.* **2005**, *102*, 6665–6670.

[30] Grimme, S. Semiempirical GGA-Type Density Functional Constructed with a Long-Range Dispersion Correction. *J. Comput. Chem.* **2006**, *27*, 1787–1799.

[31] Grimme, S.; Antony, J.; Ehrlich, S.; Krieg, H. A Consistent and Accurate *Ab Initio* Parametrization of Density Functional Dispersion Correction (DFT-D) for the 94 Elements H-Pu. *J. Chem. Phys.* **2010**, *132*, 154104.

[32] Grimme, S.; Ehrlich, S.; Goerigk, L. Effect of the Damping Function in Dispersion Corrected Density Functional Theory. *J. Comput. Chem.* **2011**, *32*, 1456–1465.

[33] Caldeweyher, E.; Ehlert, S.; Hansen, A.; Neugebauer, H.; Spicher, S.; Bannwarth, C.; Grimme, S. A Generally Applicable Atomic-charge Dependent London Dispersion Correction. *J. Chem. Phys.* **2019**, *150*, 154122.

[34] Caldeweyher, E.; Mewes, J.-M.; Ehlert, S.; Grimme, S. Extension and Evaluation of the D4 London-dispersion Model for Periodic Systems. *Phys. Chem. Chem. Phys.* **2020**, *22*, 8499–8512.

[35] Tkatchenko, A.; Scheffler, M. Accurate Molecular van der Waals Interactions From Ground-State Electron Density and Free-Atom Reference Data. *Phys. Rev. Lett.* **2009**, *102*, 073005.

[36] Tkatchenko, A.; DiStasio, Jr., R. A.; Car, R.; Scheffler, M. Accurate and Efficient Method for Many-Body van der Waals Interactions. *Phys. Rev. Lett.* **2012**, *108*, 236402.

[37] Steinmann, S. N.; Csonka, G.; Corminboeuf, C. Unified Inter-and Intramolecular Dispersion Correction Formula for Generalized Gradient Approximation Density Functional Theory. *J. Chem. Theory Comput.* **2009**, *5*, 2950–2958.

[38] Steinmann, S. N.; Corminboeuf, C. A System-dependent Density-based Dispersion Correction. *J. Chem. Theory Comput.* **2010**, *6*, 1990–2001.

[39] Steinmann, S. N.; Corminboeuf, C. A Generalized-gradient Approximation Exchange Hole Model for Dispersion Coefficients. *J. Chem. Phys.* **2011**, *134*, 044117.

[40] Steinmann, S. N.; Corminboeuf, C. Comprehensive Benchmarking of a Density-dependent Dispersion Correction. *J. Chem. Theory Comput.* **2011**, *7*, 3567–3577.

[41] Dion, M.; Rydberg, H.; Schröder, E.; Langreth, D. C.; Lundqvist, B. I. Van der Waals Density Functional for General Geometries. *Phys. Rev. Lett.* **2004**, *92*, 246401.

[42] Dion, M.; Rydberg, H.; Schröder, E.; Langreth, D.; Lundqvist, B. Erratum: van der Waals Density Functional for General Geometries [Phys. Rev. Lett. 92, 246401 (2004)]. *Phys. Rev. Lett.* **2005**, *95*, 109902.

[43] DiLabio, G. A. Accurate Treatment of van der Waals Interactions Using Standard Density Functional Theory Methods with Effective Core-type Potentials: Application to Carbon-containing Dimers. *Chem. Phys. Lett.* **2008**, *455*, 348–353.

[44] Mackie, I. D.; DiLabio, G. A. Interactions in Large, Polyaromatic Hydrocarbon Dimers: Application of Density Functional Theory with Dispersion Corrections. *J. Phys. Chem. A* **2008**, *112*, 10968–10976.

[45] Torres, E.; DiLabio, G. A. A (Nearly) Universally Applicable Method for Modeling Noncovalent Interactions Using B3LYP. *J. Phys. Chem. Lett.* **2012**, *3*, 1738–1744.

[46] DiLabio, G. A.; Koleini, M.; Torres, E. Extension of the B3LYP–dispersion-correcting Potential Approach to the Accurate Treatment of Both Inter-and Intramolecular Interactions. *Theor. Chem. Acc.* **2013**, *132*, 1389.

[47] Von Lilienfeld, O. A.; Tavernelli, I.; Rothlisberger, U.; Sebastiani, D. Optimization of Effective Atom Centered Potentials for London Dispersion Forces in Density Functional Theory. *Phys. Rev. Lett.* **2004**, *93*, 153004.

[48] Lin, I.-C.; Coutinho-Neto, M. D.; Felsenheimer, C.; von Lilienfeld, O. A.; Tavernelli, I.; Rothlisberger, U. Library of Dispersion-corrected Atom-centered Potentials for Generalized Gradient Approximation Functionals: Elements H, C, N, O, He, Ne, Ar, and Kr. *Phys. Rev. B* **2007**, *75*, 205131.

[49] DiLabio, G. A.; Otero-de-la Roza, A. Noncovalent Interactions in Density Functional Theory. *Rev. Comput. Chem.* **2016**, *29*, 1–97.

[50] Berland, K.; Cooper, V. R.; Lee, K.; Schröder, E.; Thonhauser, T.; Hyldgaard, P.; Lundqvist, B. I. Van der Waals Forces in Density Functional Theory: A Review of the vdW-DF Method. *Rep. Prog. Phys.* **2015**, *78*, 066501.

[51] Vydrov, O. A.; Van Voorhis, T. Nonlocal van der Waals Density Functional Made Simple. *Phys. Rev. Lett.* **2009**, *103*, 063004.

[52] Vydrov, O. A.; Voorhis, T. V. Nonlocal van der Waals Density Functional: The Simpler the Better. *J. Chem. Phys.* **2010**, *133*, 244103.

[53] Vydrov, O. A.; Van Voorhis, T. Benchmark Assessment of the Accuracy of Several van der Waals Density Functionals. *J. Chem. Theory Comput.* **2012**, *8*, 1929–1934.

[54] Langreth, D.; Lundqvist, B. I.; Chakarova-Käck, S. D.; Cooper, V.; Dion, M.; Hyldgaard, P.; Kelkkanen, A.; Kleis, J.; Kong, L.; Li, S.; Moses, P. G.; Murray, E.; Puzder, A.; Rydberg, H.; Schröder, E.; Thonhauser, T. A Density Functional for Sparse Matter. *J. Phys. Condens. Matter* **2009**, *21*, 084203.

[55] Zhao, Y.; Schultz, N. E.; Truhlar, D. G. Exchange-correlation Functional with Broad Accuracy for Metallic and Nonmetallic Compounds, Kinetics, and Noncovalent Interactions. *J. Chem. Phys.* **2005**, *123*, 161103.

[56] Zhao, Y.; Truhlar, D. G. A New Local Density Functional for Main-group Thermochemistry, Transition Metal Bonding, Thermochemical Kinetics, and Noncovalent Interactions. *J. Chem. Phys.* **2006**, *125*, 194101.

[57] Zhao, Y.; Truhlar, D. G. The M06 Suite of Density Functionals for Main Group Thermochemistry, Thermochemical Kinetics, Noncovalent Interactions, Excited States, and Transition Elements: Two New Functionals and Systematic Testing of Four M06-class Functionals and 12 Other Functionals. *Theor. Chem. Acc.* **2008**, *120*, 215–241.

[58] Peverati, R.; Zhao, Y.; Truhlar, D. G. Generalized Gradient Approximation That Recovers the Second-order Density-gradient Expansion with Optimized Across-the-board Performance. *J. Phys. Chem. Lett.* **2011**, *2*, 1991–1997.

[59] Peverati, R.; Truhlar, D. G. Exchange–correlation Functional With Good Accuracy for Both Structural and Energetic Properties While Depending Only on the Density and Its Gradient. *J. Chem. Theory Comput.* **2012**, *8*, 2310–2319.

[60] Ambrosetti, A.; Reilly, A. M.; DiStasio, R. A.; Tkatchenko, A. Long-range Correlation Energy Calculated from Coupled Atomic Response Functions. *J. Chem. Phys.* **2014**, *140*, 18A508.

[61] Bučko, T.; Lebègue, S.; Gould, T.; Ángyán, J. G. Many-body Dispersion Corrections for Periodic Systems: An Efficient Reciprocal Space Implementation. *J. Phys. Condens. Matter* **2016**, *28*, 045201.

[62] Becke, A. D.; Johnson, E. R. Exchange-hole Dipole Moment and the Dispersion Interaction Revisited. *J. Chem. Phys.* **2007**, *127*, 154108.

[63] Blum, V.; Gehrke, R.; Hanke, F.; Havu, P.; Havu, V.; Ren, X.; Reuter, K.; Scheffler, M. *Ab initio* Molecular Simulations with Numeric Atom-centered Orbitals. *Comput. Phys. Commun.* **2009**, *180*, 2175–2196.

[64] Havu, V.; Blum, V.; Havu, P.; Scheffler, M. Efficient O(N) Integration for All-electron Electronic Structure Calculation Using Numeric Basis Functions. *J. Comput. Phys.* **2009**, *228*, 8367–8379.

[65] Ren, X.; Rinke, P.; Blum, V.; Wieferink, J.; Tkatchenko, A.; Sanfilippo, A.; Reuter, K.; Scheffler, M. Resolution-of-identity Approach to Hartree–Fock, Hybrid Density Functionals, RPA, MP2 and GW with Numeric Atom-centered Orbital Basis Functions. *New J. Phys.* **2012**, *14*, 053020.

[66] Marek, A.; Blum, V.; Johanni, R.; Havu, V.; Lang, B.; Auckenthaler, T.; Heinecke, A.; Bungartz, H.-J.; Lederer, H. The ELPA Library: Scalable Parallel Eigenvalue Solutions for Electronic Structure Theory and Computational Science. *J. Phys. Condens. Matter* **2014**, *26*, 213201.

[67] Levchenko, S. V.; Ren, X.; Wieferink, J.; Johanni, R.; Rinke, P.; Blum, V.; Scheffler, M. Hybrid Functionals for Large Periodic Systems in an All-electron, Numeric Atom-centered Basis Framework. *Comput. Phys. Commun.* **2015**, *192*, 60–69.

[68] Huhn, W. P.; Blum, V. One-hundred-three Compound Band-structure Benchmark of Post-self-consistent Spin-orbit Coupling Treatments in Density Functional Theory. *Phys. Rev. Mater.* **2017**, *1*, 033803.

[69] Knuth, F.; Carbogno, C.; Atalla, V.; Blum, V.; Scheffler, M. All-electron Formalism for Total Energy Strain Derivatives and Stress Tensor Components for Numeric Atom-centered Orbitals. *Comput. Phys. Commun.* **2015**, *190*, 33–50.

[70] Junquera, J.; Paz, O.; Sánchez-Portal, D.; Artacho, E. Numerical Atomic Orbitals for Linear-Scaling Calculations. *Phys. Rev. B* **2001**, *64*, 235111.

[71] Dovesi, R.; Orlando, R.; Erba, A.; Zicovich-Wilson, C. M.; Civalleri, B.; Casassa, S.; Maschio, L.; Ferrabone, M.; De La Pierre, M.; D'Arco, P.; Noël, Y.; Causà, M.; Rérat, M.; Kirtman, B. CRYSTAL14: A Program for the *Ab Initio* Investigation of Crystalline Solids. *Int. J. Quantum Chem.* **2014**, *114*, 1287–1317.

[72] Dovesi, R.; Erba, A.; Orlando, R.; Zicovich-Wilson, C. M.; Civalleri, B.; Maschio, L.; Rerat, M.; Casassa, S.; Baima, J.; Salustro, S.; Kirtman, B. Quantum-Mechanical Condensed Matter Simulations with CRYSTAL. *Wiley Interdiscip. Rev.: Comput. Mol. Sci.* **2018**, *8*, e1360.

[73] Kannemann, F. O.; Becke, A. D. Van der Waals Interactions in Density-Functional Theory: Intermolecular Complexes. *J. Chem. Theory Comput.* **2010**, *6*, 1081–1088.

[74] Otero-de-la-Roza, A.; Johnson, E. R. Van der Waals Interactions in Solids Using the Exchange-Hole Dipole Moment Model. *J. Chem. Phys.* **2012**, *136*, 174109.

[75] Reilly, A. M.; Tkatchenko, A. Understanding the Role of Vibrations, Exact Exchange, and Many-Body van der Waals Interactions in the Cohesive Properties of Molecular Crystals. *J. Chem. Phys.* **2013**, *139*, 024705.

[76] Tawfik, S. A.; Gould, T.; Stampfl, C.; Ford, M. J. Evaluation of van der Waals Density Functionals for Layered Materials. *Phys. Rev. Mater.* **2018**, *2*, 034005.

[77] Björkman, T.; Gulans, A.; Krasheninnikov, A. V.; Nieminen, R. M. Van der Waals Bonding in Layered Compounds from Advanced Density-Functional First-Principles Calculations. *Phys. Rev. Lett.* **2012**, *108*, 235502.

[78] Zhang, P.; Zhang, Y.; Wei, Y.; Jiang, H.; Wang, X.; Gong, Y. Contact Engineering for Two-dimensional Semiconductors. *J. Semicond.* **2020**, *41*, 1–16.

[79] Duong, D. L.; Yun, S. J.; Lee, Y. H. Van der Waals Layered Materials: Opportunities and Challenges. *ACS Nano* **2017**, *11*, 11803–11830.

[80] Das, S.; Appenzeller, J. Where Does the Current Flow in Two-dimensional Layered Systems? *Nano Lett.* **2013**, *13*, 3396–3402.

[81] Guo, Y.; Robertson, J. Band Engineering in Transition Metal Dichalcogenides: Stacked versus Lateral Heterostructures. *Appl. Phys. Lett.* **2016**, *108*, 233104.

[82] Kang, J.; Liu, W.; Sarkar, D.; Jena, D.; Banerjee, K. Computational Study of Metal Contacts to Monolayer Transition-Metal Dichalcogenide Semiconductors. *Phys. Rev. X* **2014**, *4*, 031005.

[83] Mak, K. F.; Lee, C.; Hone, J.; Shan, J.; Heinz, T. F. Atomically Thin $\mathrm{MoS_2}$: A New Direct-Gap Semiconductor. *Phys. Rev. Lett.* **2010**, *105*, 136805.

[84] Szabo, A.; Ostlund, N. S. *Modern Quantum Chemistry: Introduction to Advanced Electronic Structure Theory*, 1st ed.; Dover Publications, Inc., 1996.

[85] Parr, R. G. Density Functional Theory. *Annu. Rev. Phys. Chem.* **1983**, *34*, 631–656.

[86] Jain, A.; Shin, Y.; Persson, K. A. Computational Predictions of Energy Materials Using Density Functional Theory. *Nat. Rev. Mater.* **2016**, *1*, 1–13.

[87] Kohn, W.; Sham, L. J. Self-Consistent Equations Including Exchange and Correlation Effects. *Phys. Rev.* **1965**, *140*, 1133.

[88] Perdew, J. P.; Wang, Y. Accurate and Simple Analytic Representation of the Electron-gas Correlation Energy. *Phys. Rev. B* **1992**, *45*, 13244–13249.

[89] Becke, A. D. Density Functional Calculations of Molecular Bond Energies. *J. Chem. Phys.* **1986**, *85*, 4524–4529.

[90] Lacks, D. J.; Gordon, R. G. Pair Interactions of Rare-gas Atoms as a Test of Exchange-energy-density Functionals in Regions of Large Density Gradients. *Phys. Rev. A* **1993**, *47*, 4681.

[91] Zhang, Y.; Pan, W.; Yang, W. Describing van der Waals Interaction in Diatomic Molecules with Generalized Gradient Approximations: The Role of the Exchange Functional. *J. Chem. Phys.* **1997**, *107*, 7921–7925.

[92] Becke, A. D.; Roussel, M. R. Exchange Holes in Inhomogeneous Systems: A Coordinate Space Model. *Phys. Rev. A* **1989**, *39*, 3761–3767.

[93] Becke, A. D. Density-Functional Thermochemistry. III. The Role of Exact Exchange. *J. Chem. Phys.* **1993**, *98*, 5648–5652.

[94] Adamo, C.; Barone, V. Toward Reliable Density Functional Methods Without Adjustable Parameters: The PBE0 Model. *J. Chem. Phys.* **1999**, *110*, 6158–6170.

[95] Bloch, F. Quantum Mechanics of Electrons in Crystal Lattices. *Z. Phys.* **1928**, *52*, 555–600.

[96] Monkhorst, H. J.; Pack, J. D. Special Points for Brillouin-Zone Integrations. *Phys. Rev. B* **1976**, *13*, 5188–5192.

[97] Hamann, D.; Schlüter, M.; Chiang, C. Norm-conserving Pseudopotentials. *Phys. Rev. Lett.* **1979**, *43*, 1494.

[98] Troullier, N.; Martins, J. A Straightforward Method for Generating Soft Transferable Pseudopotentials. *Solid State Commun.* **1990**, *74*, 613–616.

[99] Troullier, N.; Martins, J. L. Efficient Pseudopotentials for Plane-wave Calculations. *Phys. Rev. B* **1991**, *43*, 1993–2006.

[100] Blöchl, P. E. Projector Augmented-Wave Method. *Phys. Rev. B* **1994**, *50*, 17953–17979.

[101] Kresse, G.; Joubert, D. From Ultrasoft Pseudopotentials to the Projector Augmented-Wave Method. *Phys. Rev. B* **1999**, *59*, 1758–1775.

[102] Slater, J. C. Wave Functions in a Periodic Potential. *Phys. Rev.* **1937**, *51*, 846–851.

[103] Slater, J. C. In *Energy Band Calculations by the Augmented Plane Wave Method*; Löwdin, P.-O., Ed.; Advances in Quantum Chemistry; Academic Press, 1964; Vol. 1; pp 35–58.

[104] Zwanziger, J. W. Computation of NMR Observables: Consequences of Projector-Augmented Wave Sphere Overlap. *Solid State Nucl. Magn. Reson.* **2016**, *80*, 14–18.

[105] Giannozzi, P.; Andreussi, O.; Brumme, T.; Bunau, O.; Buongiorno Nardelli, M.; Calandra, M.; Car, R.; Cavazzoni, C.; Ceresoli, D.; Cococcioni, M.; Colonna, N.; Carnimeo, I.; Dal Corso, A.; de Gironcoli, S.; Delugas, P.; DiStasio, R.; Ferretti, A.; Floris, A.; Fratesi, G.; Fugallo, G.; Gebauer, R.; Gerstmann, U.; Giustino, F.; Gorni, T.; Jia, J.; Kawamura, M.; Ko, H.-Y.; Kokalj, A.; Küçükbenli, E.; Lazzeri, M.; Marsili, M.; Marzari, N.; Mauri, F.; Nguyen, N. L.; Nguyen, H.-V.; Otero-de-la-Roza, A.; Paulatto, L.; Poncé, S.; Rocca, D.; Sabatini, R.; Santra, B.; Schlipf, M.; Seitsonen, A.; Smogunov, A.; Timrov, I.; Thonhauser, T.; Umari, P.; Vast, N.; Baroni, S. Advanced Capabilities for Materials Modelling with Quantum ESPRESSO. *J. Phys.: Condens. Matter* **2017**, *29*, 465901.

[106] Jensen, S. R.; Saha, S.; Flores-Livas, J. A.; Huhn, W.; Blum, V.; Goedecker, S.; Frediani, L. The Elephant in the Room of Density Functional Theory Calculations. *J. Phys. Chem. Lett.* **2017**, *8*, 1449–1457.

[107] Mayer, I. Towards a "Chemical" Hamiltonian. *Int. J. Quantum Chem.* **1983**, *23*, 341–363.

[108] Mayer, I.; Valiron, P. Second Order Møller–Plesset Perturbation Theory Without Basis Set Superposition Error. *J. Chem. Phys.* **1998**, *109*, 3360–3373.

[109] Boys, S. F.; Bernardi, F. The Calculation of Small Molecular Interactions by the Differences of Separate Total Energies. Some Procedures with Reduced Errors. *Mol. Phys.* **1970**, *19*, 553–566.

[110] Kruse, H.; Grimme, S. A Geometrical Correction for the Inter-and Intra-Molecular Basis Set Superposition Error in Hartree-Fock and Density Functional Theory Calculations for Large Systems. *J. Chem. Phys.* **2012**, *136*, 154101.

[111] Brandenburg, J. G.; Alessio, M.; Civalleri, B.; Peintinger, M. F.; Bredow, T.; Grimme, S. Geometrical Correction for the Inter- and Intramolecular Basis Set Superposition Error in Periodic Density Functional Theory Calculations. *J. Phys. Chem. A* **2013**, *117*, 9282–9292.

[112] Grimme, S.; Brandenburg, J. G.; Bannwarth, C.; Hansen, A. Consistent Structures and Interactions by Density Functional Theory with Small Atomic Orbital Basis Sets. *J. Chem. Phys.* **2015**, *143*, 054107.

[113] Van Lenthe, E.; Baerends, E. J. Optimized Slater-type Basis Sets for the Elements 1–118. *J. Comput. Chem.* **2003**, *24*, 1142–1156.

[114] Hehre, W. J.; Stewart, R. F.; Pople, J. A. Self-consistent Molecular-orbital Methods. I. Use of Gaussian Expansions of Slater-type Atomic Orbitals. *J. Chem. Phys.* **1969**, *51*, 2657–2664.

[115] Hehre, W. J.; Ditchfield, R.; Stewart, R. F.; Pople, J. A. Self-Consistent Molecular Orbital Methods. IV. Use of Gaussian Expansions of Slater-Type Orbitals. Extension to Second-Row Molecules. *J. Chem. Phys.* **1970**, *52*, 2769–2773.

[116] Pople, J. A.; Head-Gordon, M.; Fox, D. J.; Raghavachari, K.; Curtiss, L. A. Gaussian-1 Theory: A General Procedure for Prediction of Molecular Energies. *J. Chem. Phys.* **1989**, *90*, 5622–5629.

[117] Curtiss, L. A.; Jones, C.; Trucks, G. W.; Raghavachari, K.; Pople, J. A. Gaussian-1 Theory of Molecular Energies for Second-Row Compounds. *J. Chem. Phys.* **1990**, *93*, 2537–2545.

[118] Wilson, A. K.; van Mourik, T.; Dunning Jr, T. H. Gaussian Basis Sets for Use in Correlated Molecular Calculations. VI. Sextuple Zeta Correlation Consistent Basis Sets for Boron Through Neon. *J. Mol. Struc-Theochem* **1996**, *388*, 339–349.

[119] Zunger, A.; Freeman, A. J. Self-consistent Numerical-basis-set Linear-combination-of-atomic-orbitals Model for the Study of Solids in the Local Density Formalism. *Phys. Rev. B* **1977**, *15*, 4716–4737.

[120] Delley, B.; Ellis, D. E. Efficient and Accurate Expansion Methods for Molecules in Local Density Models. *J. Chem. Phys.* **1982**, *76*, 1949–1960.

[121] Delley, B. An All-electron Numerical Method for Solving the Local Density Functional for Polyatomic Molecules. *J. Chem. Phys.* **1990**, *92*, 508–517.

[122] Averill, F.; Ellis, D. E. An Efficient Numerical Multicenter Basis Set for Molecular Orbital Calculations: Application to $FeCl_4$. *J. Comput. Phys.* **1973**, *59*, 6412–6418.

[123] Becke, A. D. A Multicenter Numerical Integration Scheme for Polyatomic Molecules. *J. Chem. Phys.* **1988**, *88*, 2547–2553.

[124] Slater, J. C. Atomic Radii in Crystals. *J. Chem. Phys.* **1964**, *41*, 3199–3204.

[125] Otero-de-la-Roza, A.; Johnson, E. R. A Benchmark for Non-Covalent Interactions in Solids. *J. Chem. Phys.* **2012**, *137*, 054103.

[126] Salem, L. The Calculation of Dispersion Forces. *Mol. Phys.* **1960**, *3*, 441–452.

[127] Hirshfeld, F. L. Bonded-Atom Fragments for Describing Molecular Charge Densities. *Theoret. Chim. Acta* **1997**, *44*, 129–138.

[128] Heidar-Zadeh, F.; Ayers, P. W.; Verstraelen, T.; Vinogradov, I.; Vöhringer-Martinez, E.; Bultinck, P. Information-Theoretic Approaches to Atoms-in-Molecules: Hirshfeld Family of Partioning Schemes. *J. Phys. Chem. A* **2018**, *122*, 4219–4245.

[129] Becke, A. D. A Real-space Model of Nondynamical Correlation. *J. Chem. Phys.* **2003**, *119*, 2972–2977.

[130] Becke, A. D.; Johnson, E. R. A Density-Functional Model of the Dispersion Interaction. *J. Chem. Phys.* **2005**, *123*, 154101.

[131] Gil, A.; Segura, J.; Temme, N. M. *Numerical Methods for Special Functions*; SIAM, 2007.

[132] Koide, A. A New Expansion for Dispersion Forces and Its Application. *J. Phys. B* **1976**, *9*, 3173.

[133] Johnson, E. R.; Becke, A. D. A Post-Hartree-Fock Model of Intermolecular Interactions: Inclusion of Higher-Order Corrections. *J. Chem. Phys.* **2006**, *124*, 174104.

[134] Christian, M. S.; Otero-de-la-Roza, A.; Johnson, E. R. Surface Adsorption From the Exchange-hole Dipole Moment Dispersion Model. *J. Chem. Theory Comput.* **2016**, *12*, 3305–3315.

[135] Christian, M. S.; Otero-de-la-Roza, A.; Johnson, E. R. Adsorption of Graphene to Nickel (111) Using the Exchange-Hole Dipole Moment Model. *Carbon* **2017**, *118*, 184–191.

[136] Christian, M. S.; Otero-de-la-Roza, A.; Johnson, E. R. Adsorption of Graphene to Metal (111) Surfaces Using the Exchange-Hole Dipole Moment Model. *Carbon* **2017**, *124*, 531–540.

[137] Grimme, S. Accurate Description of van der Waals Complexes by Density Functional Theory Including Empirical Corrections. *J. Comput. Chem.* **2004**, *25*, 1463–1473.

[138] Caldeweyher, E.; Bannwarth, C.; Grimme, S. Extension of the D3 Dispersion Coefficient Model. *J. Chem. Phys.* **2017**, *147*, 034112.

[139] Bučko, T.; Lebègue, S.; Hafner, J.; Ángyán, J. G. Tkatchenko-Scheffler van der Waals Correction Method With and Without Self-Consistent Screening Applied to Solids. *Phys. Rev. B* **2013**, *87*, 064110.

[140] Ambrosetti, A.; Reilly, A. M.; DiStasio, Jr., R. A.; Tkatchenko, A. Long-Range Correlation Energy Calculated From Coupled Atomic Response Functions. *J. Chem. Phys.* **2014**, *140*, 18A508.

[141] DiStasio Jr., R. A.; Gobre, V. V.; Tkatchenko, A. Many-Body van der Waals Interactions in Molecules and Condensed Matter. *J. Phys.: Condens. Matter* **2014**, *26*, 213202.

[142] Lee, K.; Murray, E. D.; Kong, L.; Lundqvist, B. I.; Langreth, D. C. Higher-Accuracy van der Waals Density Functional. *Phys. Rev. B* **2010**, *82*, 081101.

[143] National Research Council; Division on Engineering and Physical Sciences; Commission on Physical Sciences, Mathematics, and Applications; Panel on New Directions in Catalytic Science and Technology, *Catalysis Looks to the Future*; National Academies Press, 1992.

[144] Dumesic, J. A.; Huber, G. W.; Boudart, M. Principles of Heterogeneous Catalysis. *Handbook of Heterogeneous Catalysis: Online* **2008**, 1–15.

[145] Armor, J. N. New Catalytic Technology Commercialized in the USA During the 1990s. *Appl. Catal. A: Gen.* **2001**, *222*, 407–426.

[146] Chorkendorff, I.; Niemantsverdriet, J. W. *Concepts of Modern Catalysis and Kinetics*; John Wiley & Sons, 2017.

[147] Bartholomew, C. H.; Farrauto, R. J. *Fundamentals of Industrial Catalytic Processes*; John Wiley & Sons, 2011.

[148] Averill, B. A.; Moulijn, J. A.; van Santen, R. A.; van Leeuwen, P. W. N. M. *Catalysis: An Integrated Approach*; Elsevier, 1999.

[149] Krull, C.; Castelli, M.; Hapala, P.; Kumar, D.; Tadich, A.; Capsoni, M.; Edmonds, M.; Hellerstedt, J.; Burke, S.; Jelinek, P. Iron-based Trinuclear Metal-organic Nanostructures on a Surface with Local Charge Accumulation. *Nat. Comm.* **2018**, *9*, 1–7.

[150] Schiffrin, A.; Capsoni, M.; Farahi, G.; Wang, C.; Krull, C.; Castelli, M.; Roussy, T.; Cochrane, K.; Yin, Y.; Medhekar, N.; M., F.; Shaw, A.; Ji, W.; Burke, S. Designing Optoelectronic Properties by On-Surface Synthesis: Formation and Electronic Structure of an Iron-Terpyridine Macromolecular Complex. *ACS Nano* **2018**, *12*, 6545–6553.

[151] Valero, M. C.; Raybaud, P.; Sautet, P. Interplay Between Molecular Adsorption and Metal–support Interaction For Small Supported Metal Clusters: CO and C_2H_4 Adsorption on Pd_4/γ-Al_2O_3. *J. Cata.* **2007**, *247*, 339–355.

[152] Cyr, D. M.; Venkataraman, B.; Flynn, G. W. STM Investigations of Organic Molecules Physisorbed at the Liquid-Solid Interface. *Chem. Mater.* **1996**, *8*, 1600–1615.

[153] Grinter, D.; Thornton, G. In *Encyclopedia of Interfacial Chemistry*; Wandelt, K., Ed.; Elsevier: Oxford, 2018; pp 62–85.

[154] Grimme, S. Semiempirical GGA-type Density Functional Constructed With a Long-range Dispersion Correction. *J. Comput. Chem.* **2006**, *27*, 1787–1799.

[155] Grimme, S.; Antony, J.; Ehrlich, S.; Krieg, H. A Consistent and Accurate Ab Initio Parametrization of Density Functional Dispersion Correction (DFT-D) for the 94 Elements H-Pu. *J. Chem. Phys.* **2010**, *132*, 154104.

[156] Tkatchenko, A.; Scheffler, M. Accurate Molecular van der Waals Interactions from Ground-state Electron Density and Free-atom Reference Data. *Phys. Rev. Lett.* **2009**, *102*, 073005.

[157] Binnig, G.; Rohrer, H.; Gerber, C.; Weibel, E. Tunneling Through a Controllable Vacuum Gap. *Appl. Phys. Lett.* **1982**, *40*, 178–180.

[158] Binnig, G.; Rohrer, H.; Gerber, C.; Weibel, E. Surface Studies by Scanning Tunneling Microscopy. *Phys. Rev. Lett.* **1982**, *49*, 57–61.

[159] Tersoff, J.; Hamann, D. R. Theory of the Scanning Tunneling Microscope. *Phys. Rev. B* **1985**, *31*, 805–813.

[160] Bardeen, J. Tunnelling from a Many-Particle Point of View. *Phys. Rev. Lett.* **1961**, *6*, 57–59.

[161] Otero-de-la-Roza, A.; Johnson, E. R.; Luaña, V. CRITIC2: A Program for Real-Space Analysis of Quantum Chemical Interactions in Solids. *Comput. Phys. Commun.* **2014**, *185*, 1007–1018.

[162] Blöchl, P. E. Projector Augmented-Wave Method. *Phys. Rev. B* **1994**, *50*, 17953–17979.

[163] DeJong, M.; Price, A. J.; Mårsell, E.; Nguyen, G.; Johnson, E. R.; Burke, S. A. Small Molecule Binding to Surface-Supported Single-Sight Reaction Centers. **2020**, Manuscript in preparation.

[164] Liu, W.; Maaß, F.; Willenbockel, M.; Bronner, C.; Schulze, M.; Soubatch, S.; Tautz, F. S.; Tegeder, P.; Tkatchenko, A. Quantitative Prediction of Molecular Adsorption: Structure and Binding of Benzene on Coinage Metals. *Phys. Rev. Lett.* **2015**, *115*, 036104.

[165] Schulman, D. S.; Arnold, A. J.; Das, S. Contact Engineering for 2D Materials and Devices. *Chem. Soc. Rev.* **2018**, *47*, 3037–3058.

[166] Cheiwchanchamnangij, T.; Lambrecht, W. R. L. Quasiparticle Band Structure Calculation of Monolayer, Bilayer, and Bulk MoS_2. *Phys. Rev. B* **2012**, *85*, 205302.

[167] Kam, K. K.; Parkinson, B. A. Detailed Photocurrent Spectroscopy of the Semiconducting Group VIB Transition Metal Dichalcogenides. *J. Phys. Chem.* **1982**, *86*, 463–467.

[168] Splendiani, A.; Sun, L.; Zhang, Y.; Li, T.; Kim, J.; Chim, C.-Y.; Galli, G.; Wang, F. Emerging Photoluminescence in Monolayer MoS_2. *Nano Lett.* **2010**, *10*, 1271–1275.

[169] Ouyang, B.; Xiong, S.; Jing, Y. Tunable Phase Stability and Contact Resistance of Monolayer Transition Metal Dichalcogenides Contacts with Metal. *NPJ 2D Mater. Appl.* **2018**, *2*, 1–8.

[170] Das, S.; Chen, H.-Y.; Penumatcha, A. V.; Appenzeller, J. High Performance Multilayer MoS_2 Transistors with Scandium Contacts. *Nano Lett.* **2013**, *13*, 100–105.

[171] Liu, H.; Neal, A. T.; Ye, P. D. Channel Length Scaling of MoS_2 MOSFETs. *ACS Nano* **2012**, *6*, 8563–8569.

[172] Liu, H.; Si, M.; Najmaei, S.; Neal, A. T.; Du, Y.; Ajayan, P. M.; Lou, J.; Ye, P. D. Statistical Study of Deep Submicron Dual-gated Field-effect Transistors on Monolayer Chemical Vapor Deposition Molybdenum Disulfide Films. *Nano Lett.* **2013**, *13*, 2640–2646.

[173] Allain, A.; Kang, J.; Banerjee, K.; Kis, A. Electrical contacts to two-dimensional semiconductors. *Nature Mater.* **2015**, *14*, 1195–1205.

[174] Sze, S. M.; Ng, K. K. *Physics of Semiconductor Devices*; John Wiley & Sons, 2006.

[175] Heine, V. Theory of Surface States. *Phys. Rev.* **1965**, *138*, A1689.

[176] Soler, J. M.; Artacho, E.; Gale, J. D.; García, A.; Junquera, J.; Ordejón, P.; Sánchez-Portal, D. The SIESTA Method for *Ab Initio* Order-*N* Materials Simulation. *J. Phys.: Condens. Matter* **2002**, *14*, 2745–2779.

[177] Artacho, E.; Gale, J. D.; García, A.; Junquera, J.; Martin, R. M.; Ordejón, P.; Pruneda, J. M.; Sánchez-Portal, D.; Soler, J. M. The SIESTA Method; Developments and Applicability. *J. Phys.: Condens. Matter* **2008**, *20*, 064208.

[178] LeBlanc, L. M.; Weatherby, J. A.; Otero-de-la Roza, A.; Johnson, E. R. Non-Covalent Interactions in Molecular Crystals: Exploring the Accuracy of the Exchange-Hole Dipole Moment Model with Local Orbitals. *J. Chem. Theory Comput.* **2018**, *14*, 5715–5724.

[179] Weatherby, J. A. Unpublished results.

[180] Otero-de-la-Roza, A.; Johnson, E. R. Non-Covalent Interactions and Thermochemistry using XDM-Corrected Hybrid and Range-Separated Hybrid Density Functionals. *J. Chem. Phys.* **2013**, *138*, 204109.

[181] Christian, M. S.; Otero-de-la-Roza, A.; Johnson, E. R. Surface Adsorption from the Exchange-Hole Dipole Moment Dispersion Model. *J. Chem. Theory Comput.* **2016**, *12*, 3305–3315.

[182] Becke, A. D.; Dickson, R. M. Numerical-Solution of Schrodinger-Equation in Polyatomic-Molecules. *J. Chem. Phys.* **1990**, *92*, 3610–3612.

[183] Frisch, M. J.; Trucks, G. W.; Schlegel, H. B.; Scuseria, G. E.; Robb, M. A.; Cheeseman, J. R.; Scalmani, G.; Barone, V.; Mennucci, B.; Petersson, G. A.; Nakatsuji, H.; Caricato, M.; Li, X.; Hratchian, H. P.; Izmaylov, A. F.; Bloino, J.; Zheng, G.; Sonnenberg, J. L.; Hada, M.; Ehara, M.; Toyota, K.; Fukuda, R.; Hasegawa, J.; Ishida, M.; Nakajima, T.; Honda, Y.; Kitao, O.; Nakai, H.; Vreven, T.; Montgomery, J. A., Jr.; Peralta, J. E.; Ogliaro, F.; Bearpark, M.; Heyd, J. J.; Brothers, E.; Kudin, K. N.; Staroverov, V. N.; Kobayashi, R.; Normand, J.; Raghavachari, K.; Rendell, A.; Burant, J. C.; Iyengar, S. S.; Tomasi, J.; Cossi, M.; Rega, N.; Millam, J. M.; Klene, M.; Knox, J. E.; Cross, J. B.; Bakken, V.; Adamo, C.; Jaramillo, J.; Gomperts, R.; Stratmann, R. E.; Yazyev, O.; Austin, A. J.; Cammi, R.; Pomelli, C.; Ochterski, J. W.; Martin, R. L.; Morokuma, K.; Zakrzewski, V. G.; Voth, G. A.; Salvador, P.; Dannenberg, J. J.; Dapprich, S.; Daniels, A. D.; Farkas, O.; Foresman, J. B.; Ortiz, J. V.; Cioslowski, J.; Fox, D. J. Gaussian 09 Revision B.01. Gaussian Inc. Wallingford CT 2010.

[184] Kannemann, F. O.; Becke, A. D. Atomic Volumes and Polarizabilities in Density-Functional Theory. *J. Chem. Phys.* **2012**, *136*, 034109.

[185] Parrish, R. M.; Burns, L. A.; Smith, D.; Simmonett, A. C.; DePrince, A. E.; Hohenstein, E. G.; Bozkaya, U.; Sokolov, A. Y.; Di Remigio, R.; Richard, R. M. Psi4 1.1: An Open-Source Electronic Structure Program Emphasizing Automation, Advanced Libraries, and Interoperability. *J. Chem. Theory Comput.* **2017**, *13*, 3185–3197.

[186] Perdew, J. P.; Ernzerhof, M.; Burke, K. Rationale for Mixing Exact Exchange with Density Functional Approximations. *J. Chem. Phys.* **1996**, *105*, 9982–9985.

[187] Otero-de-la Roza, A.; LeBlanc, L. M.; Johnson, E. R. Dispersion XDM with Hybrid Functionals: Delocalization Error and Halogen Bonding in Molecular Crystals. *J. Chem. Theory Comput.* **2019**, *15*, 4933–4944.

[188] Heyd, J.; Scuseria, G. E.; Ernzerhof, M. Hybrid Functionals Based on a Screened Coulomb Potential. *J. Chem. Phys.* **2003**, *118*, 8207–8215.

[189] Hoja, J.; Tkatchenko, A. First-principles stability ranking of molecular crystal polymorphs with the DFT+ MBD approach. *Faraday Discuss.* **2018**, *211*, 253–274.

[190] Marom, N.; Tkatchenko, A.; Scheffler, M.; Kronik, L. Describing Both Dispersion Interactions and Electronic Structure Using Density Functional Theory: The Case of Metal-Phthalocyanine Dimers. *J. Chem. Theory Comput.* **2010**, *6*, 81–90.

[191] Marom, N.; Tkatchenko, A.; Rossi, M.; Gobre, V. V.; Hod, O.; Scheffler, M.; Kronik, L. Dispersion Interactions with Density-functional Theory: Benchmarking Semiempirical and Interatomic Pairwise Corrected Density Functionals. *J. Chem. Theory Comput.* **2011**, *7*, 3944–3951.

[192] Riley, K. E.; Pitonňák, M.; Jurečka, P.; Hobza, P. Stabilization and Structure Calculations for Noncovalent Interactions in Extended Molecular Systems Based on Wave Function and Density Functional Theories. *Chem. Rev.* **2010**, *110*, 5023–5063.

[193] Grimme, S. Supramolecular Binding Thermodynamics by Dispersion-Corrected Density Functional Theory. *Chem. Eur. J.* **2012**, *18*, 9955–9964.

[194] Sabatini, R.; Gorni, T.; De Gironcoli, S. Nonlocal van der Waals Density Functional Made Simple and Efficient. *Phys. Rev. B* **2013**, *87*, 041108.

[195] Lebègue, S.; Eriksson, O. Electronic Structure of Two-dimensional Crystals from Ab Initio Theory. *Phys. Rev. B* **2009**, *79*, 115409.

[196] Wu, W.; Wang, L.; Yu, R.; Liu, Y.; Wei, S.-H.; Hone, J.; Wang, Z. L. Piezophototronic Effect in Single-atomic-layer MoS_2 for Strain-gated Flexible Optoelectronics. *Adv. Mater.* **2016**, *28*, 8463–8468.

[197] Saidi, W. A. Influence of Strain and Metal Thickness on Metal-MoS_2 Contacts. *J. Chem. Phys.* **2014**, *141*, 094707.

[198] Dye, J. L. Electrides: Early Examples of Quantum Confinement. *Acc. Chem. Res.* **2009**, *42*, 1564–1572.

[199] Dale, S. G.; Johnson, E. R. Theoretical Descriptors of Electrides. *J. Phys. Chem. A* **2018**, *122*, 9371–9391.

[200] Lee, K.; Kim, S. W.; Toda, Y.; Matsuishi, S.; Hosono, H. Dicalcium Nitride as a Two-dimensional Electride with an Anionic Electron Layer. *Nature* **2013**, *494*, 336–340.

[201] Kim, S.; Song, S.; Park, J.; Yu, H. S.; Cho, S.; Kim, D.; Baik, J.; Choe, D.-H.; Chang, K. J.; Lee, Y. H.; Kim, S. W.; Yang, H. Long-range Lattice Engineering of $MoTe_2$ by a 2D Electride. *Nano Lett.* **2017**, *17*, 3363–3368.

[202] Kaadou, F.; Maassen, J.; Johnson, E. R. Unpublished Results.